Journal of Marine Systems 133 (2014) 39–54

Contents lists available at ScienceDirect

Journal of Marine Systems

journal homepage: www.elsevier.com/locate/jmarsys

Connecting Atlantic temperature variability and biological cycling in two earth system models

Anand Gnanadesikan [a,*], John P. Dunne [b], Rym Msadek [b]

[a] Johns Hopkins University, Baltimore, MD USA
[b] Geophysical Fluid Dynamics Laboratory, Princeton, NJ USA

ARTICLE INFO

Article history:
Received 17 May 2012
Received in revised form 16 September 2013
Accepted 20 October 2013
Available online 26 October 2013

Keywords:
Atlantic meridional overturning
Primary productivity
Decadal variability
Earth system modeling

ABSTRACT

Connections between the interdecadal variability in North Atlantic temperatures and biological cycling have been widely hypothesized. However, it is unclear whether such connections are due to small changes in basin-averaged temperatures indicated by the Atlantic Multidecadal Oscillation (AMO) Index, or whether both biological cycling and the AMO index are causally linked to changes in the Atlantic Meridional Overturning Circulation (AMOC). We examine interdecadal variability in the annual and month-by-month diatom biomass in two Earth System Models with the same formulations of atmospheric, land, sea ice and ocean biogeochemical dynamics but different formulations of ocean physics and thus different AMOC structures and variability. In the isopycnal-layered ESM2G, strong interdecadal changes in surface salinity associated with changes in AMOC produce spatially heterogeneous variability in convection, nutrient supply and thus diatom biomass. These changes also produce changes in ice cover, shortwave absorption and temperature and hence the AMO Index. Off West Greenland, these changes are consistent with observed changes in fisheries and support climate as a causal driver. In the level-coordinate ESM2M, nutrient supply is much higher and interdecadal changes in diatom biomass are much smaller in amplitude and not strongly linked to the AMO index.

1. Introduction

Changes in the mean sea surface temperature of the Atlantic have been associated with climate shifts around the northern hemisphere (Schlesinger and Ramankutty, 1994), and are sometimes referred to as the Atlantic Multidecadal Oscillation (AMO). Enfield et al. (2001) proposed an AMO index, corresponding to the decadally-smoothed mean temperature of the Atlantic between the equator and 70°N, and showed that this index is correlated with rainfall over the Mississippi basin and Southern Florida. Locally, changes in ocean temperature have also been linked to ecosystem shifts, including changes in the Atlantic cod (*Gadus morhua*) fishery off of Greenland (Jensen, 1939; Stein, 2007) and Norway (Sundby and Nakken, 2008) and changes in species composition in a number of locations (Collie et al., 2008 in Narragansett Bay; Dulvy et al., 2008 in the North Sea; Nye et al., 2009, in the Mid-Atlantic Bight). The ICES/PICES workshop on the AMO leading to this special issue was convened in part to evaluate whether these changes could be linked to the AMO index, and whether such a linkage might provide some level of predictability. However, the relatively short record of Atlantic temperatures makes it unclear whether the AMO is truly an oscillation with a well-defined autocorrelation (in which case knowledge of the AMO index would provide a high degree of predictability) or simply reflects red-noise variability (in which case it would not). In order to sidestep this question we will use the AMO index as a measure of the state of the Atlantic circulation and examine the degree to which it varies synchronously with ocean ecosystems.

It is far from clear that local changes in SST and ecosystems should be directly related to the relatively small changes in basin-averaged SST associated with the AMO index. While possible mechanisms invoked in, for example Nye et al., 2009, include changes in the optimal temperature range for various species, the AMO index is associated with O(0.1–0.2 °C) changes in the basin-mean decadal temperature (Sutton and Hodson, 2005). Given that north–south temperature gradients average ~0.3–0.4 °C per degree latitude, it is hard to see that such small changes should produce first-order effects on ecosystems.

However, it is also likely that the AMO index is a proxy for other changes more directly relevant to biological cycling. In numerical models, the AMO index is closely related to the Atlantic Meridional Overturning Circulation, (Delworth and Mann, 2000). This means that changes in the AMO index may be the result of large-scale reorganizations of the circulation which both change the transport of heat into the basin and the release of that heat to the atmosphere. Additionally, when Zhang and Delworth (2006) modeled the impact of such changes in meridional ocean heat transport on climate they found interdecadal changes in rainfall over Africa and India and changes in vertical wind shear sufficient to alter tropical cyclone activity over the Atlantic. Such indirect impacts of changes in Atlantic SSTs may be important for various ecosystems.

* Corresponding author at: 327 Olin Hall, Department of Earth and Planetary Sciences, Johns Hopkins University, 3400 N. Charles St., Baltimore, MD USA 21218.
E-mail addresses: gnanades@jhu.edu (A. Gnanadesikan), john.dunne@noaa.gov (J.P. Dunne), rym.msadek@noaa.gov (R. Msadek).

0924-7963/$ – see front matter © 2013 Elsevier B.V. All rights reserved.
http://dx.doi.org/10.1016/j.jmarsys.2013.10.003

A complication in representing the overturning in models is that the results are known to depend on the vertical coordinate system used in the ocean. In a study of the North Atlantic Willebrand et al. (2001) compared the standard level coordinate model used in global climate simulations since the 1970s to a terrain-following sigma coordinate model and an isopycnal model using layer coordinates. While all three models produced an AMOC of 16–20 Sv, the details of where the downwelling occurred and how rapidly the sinking waters are recycled varied significantly between the models. The isopycnal model was the only one of the three that was capable of reproducing both the magnitude of the AMOC and the heat transport associated with it. One reason for the difference is that the level coordinate models used in most global coupled climate models have trouble representing the deep overflows found downstream of the Denmark Strait, Iceland–Scotland ridge, and Faeroe Bank Channel (Legg et al., 2006; Winton et al., 1998), entraining too much light water near the top of the overflow and failing to preserve the characteristics of dense water as it enters the interior. Additionally, it became clear that such models were potentially prone to high levels of numerical diffusion causing excessive upwelling in lower latitudes. Over the past decades these facts have motivated efforts both to make level coordinate models less diffusive (i.e. Griffies et al., 1998) and to develop layer coordinate models into proper tools for climate simulation.

This paper thus has two primary goals. The first is to evaluate the linkages between the AMO index, interdecadal changes in AMOC and interdecadal biological variability in Earth System Models that represent the coupling between atmosphere, ocean, land, sea ice and ecosystems. The second is to see whether these linkages are robust across different formulations of ocean physics. Thus the two Earth System Models we use, developed by the Geophysical Fluid Dynamics Laboratory, have identical representation of atmosphere and both terrestrial and oceanic ecosystems, but use different codes to simulate the ocean. In the model denoted ESM2M the ocean is simulated using the GFDL Modular Ocean Model (MOM4) which uses a vertical discretization in which the ocean volume is broken up into boxes which represent ranges in pressure/depth. The model denoted ESM2G, uses the Generalized Ocean Layer Dynamics code (GOLD) an isopycnal formulation in which the vertical discretization consists of variable-depth layers which in the interior correspond to layers of constant potential density.

The structure of this paper is as follows. In the following section, we briefly sketch the important components of our physical and biogeochemical models. In Section 3, we examine the variability of the AMO index in the models, and consider its connection to the overturning circulation. In Section 4, we continue by looking at the connection between the AMO index and large diatom biomass, and show that this is very different between the two models. We examine how differences in the baseline biogeochemical simulation as well as differences in the drivers of temperature variability in the Atlantic in the two models result in these different behaviors.

2. Methods

2.1. Physical models

The atmospheric, land surface and sea-ice components of the Earth System Model used in this paper originated from that used in the GFDL CM2.1 series (Delworth et al., 2006; Gnanadesikan et al., 2006) and are described in detail in Dunne et al. (2012). The atmospheric model has a resolution of $2 \times 2.5^\circ$ and 24 vertical levels, with six of them in the lower boundary layer. Two ocean models are used. ESM2M uses the pressure-coordinate code MOM4.1 (Dunne et al., 2012; Griffies, 2009; Griffies et al., 2005), with up-to-date parameterizations of mixed-layer dynamics and mesoscale eddy mixing (Ferrari et al., 2010), and a new parameterization of submesoscale mixing (Fox-Kemper et al., 2011). Vertical diffusion in the deep ocean uses the Simmons et al. (2004) parameterization which links turbulent mixing coefficients to the rate of internal wave generation by the barotropic tides.

ESM2G uses the Generalized Ocean Layer Dynamics (GOLD) code (Dunne et al., 2012; Hallberg, 1995; Hallberg and Adcroft, 2009), configured as an isopycnal layer model in the ocean interior with a four layer surface layer. Earlier versions of this model are reported in Harrison and Hallberg (2008) and Gnanadesikan and Anderson (2009). Differences between previous versions of the GOLD model and the one used in this code include the implementation of the Simmons et al. (2004) deep tidal diffusion, implementation of a lower background diapycnal diffusion near the equator following Harrison and Hallberg (2008) and implementation of the mixed-layer restratification of Fox-Kemper et al. (2011). A potentially significant difference between ESM2G and ESM2M is that ESM2G uses an isopycnal tracer diffusion coefficient which varies spatially over a range of 50–900 $m^2\ s^{-1}$ depending on the buoyancy frequency and isopycnal slope while ESM2M uses a constant one of 600 $m^2\ s^{-1}$. This coefficient determines the lateral stirring by mesoscale eddies of all prognostic tracers in the model, including nutrients, oxygen, phytoplankton, temperature and salinity. In the absence of feedbacks on circulation, we would expect higher isopycnal tracer diffusion coefficients to prevent nutrients from accumulating in stagnant low-latitude oxygen minimum zones, reducing the productivity of the low latitudes and raising productivity in high latitudes. Mesoscale eddies also produce advective fluxes. Following Gent and McWilliams (1990), these fluxes are represented as flattening isopycnal surfaces, using a spatially variable thickness diffusion coefficient that depends on the local thermal wind shear (Gnanadesikan et al., 2006). ESM2G has a slightly larger range for this coefficient (10 $m^2\ s^{-1}$–900 $m^2\ s^{-1}$) than ESM2M (100–800 $m^2 s^{-1}$). In general, higher thickness diffusion would be expected to reduce mixed-layer depths, particularly in high latitudes (Gnanadesikan et al., 2007).

The models handle mixed-layers differently. ESM2M uses the KPP mixed-layer scheme of Large et al. (1994) which diagnoses a mixed-layer depth based on surface fluxes and stratification. However, the effective mixed-layer depth in this scheme can never be smaller than the thickness of the topmost box, which is of order 10 m. By contrast, ESM2G uses the four-layer, total kinetic energy budget, bulk scheme described in Hallberg (2003) in which the top two variable-density layers are completely mixed with respect to tracer but not with respect to velocity and two transition layers govern exchange with the isopycnal interior. ESM2G thus allows for a continuously varying mixed-layer depth which can take any value greater than 2 m and should thus be superior to ESM2M in treating such shallow mixed layers. However, insofar as processes such as breaking waves are not included in the mixed layer energy balance the result may be to make ESM2G too sensitive to addition of buoyancy under calm winds. Additionally, the use of variable-depth mixed layers does introduce some complications. When the mixed layer shallows as a result of surface buoyancy addition, the water detrained from the mixed layer may not be at a density that corresponds to that of one of the interior layers. To avoid dividing the detrained water between two interior density layers (essentially "unmixing" the detrained fluid), the model instead adds the detrained water to a variable-density interior transition layer, which detrains slowly into a second variable-density transition layer. This in turn detrains into a constant-density interior layer once it matches the density of this layer. This scheme allows for much smoother interaction between the surface layers and the interior, so that water detrained from a rapidly lightening surface layer will eventually be distributed over the entire range of densities found at the surface. However, it lacks resolution of the sub-mixed-layer euphotic zone under conditions of weakly-stratified interior layers, the primary shortcoming of isopycnal models.

Dunne et al. (2012) examine the physical differences between ESM2M and ESM2G. We briefly summarize their results here. The patterns of radiative biases relative to observations (shortwave albedo at the top of the atmosphere, downward shortwave radiation at the surface, surface albedo) are very similar between the two models. Biases in sea surface temperature and salinity are also similar, though ESM2G

tends to have somewhat larger RMS biases than ESM2M. In the ocean interior, however, the models differ considerably. ESM2M tends to drift warm, producing a thermocline that is excessively deep. ESM2G, by contrast, tends to drift slightly cold in the deep ocean and to produce a thermocline that is somewhat too thin. Overturning circulations within the two models are broadly similar in magnitude. The annual-mean maximum Atlantic overturning in density space at 26°N in ESM2G is 20.5 Sv +/− 1.5 Sv while in ESM2M it is 21.1 Sv +/− 1.5Sv. Both models compare relatively well with the latest observational estimates from RAPID that give a maximum overturning at 26.5°N equal to 18.7 +/− 4.8 Sv (Rayner et al., 2011). A somewhat more powerful way of assessing the overall ventilation of the Atlantic is the ideal age, a tracer that is set to zero at the surface and ages at a rate of 1 yr/yr below the surface (Thiele and Sarmiento, 1990). Ideal age measures the average time required to reach an interior box from the surface and accounts for diffusive and advective pathways associated with the overturning. ESM2G produces a relatively old mass of intermediate waters within the Atlantic, with peak ages reaching 800 years in the Southern Hemisphere, overlying a relatively well-ventilated deep ocean in which ages range from 100 to 500 years. ESM2M produces a more-ventilated intermediate water, with ages of around 600 years, but has much shallower ventilation in the North Atlantic, so that the deep waters there are significantly older, ranging from 300 to 500 years. In both models a significant fraction of the northern overturning is fed from the Southern Ocean, but the northern and southern cells are deeper in ESM2G than in ESM2M, with the northern cell realistically penetrating all the way to the bottom in the North Atlantic in ESM2G.

We extend this analysis by looking at the climate of the Atlantic during the month of March, when ice extent and mixed-layer depths are at their maxima. The observed mixed-layers (Fig. 1A) from the Argo dataset (Holte et al., 2010) show two tongues of high values, one which underlies a region of strong southwesterly winds running from southwest to northeast across the Atlantic, and another region along the northern and eastern boundaries of the main Atlantic basin extending into the Labrador Sea. The two models reproduce this pattern qualitatively, however, the level-coordinate ESM2M model predicts excessively deep (>1500 m) mixed-layers in both the Northeast Atlantic and the Labrador Sea (Fig. 1C). The layer-coordinate ESM2G has much shallower mixed-layers in both

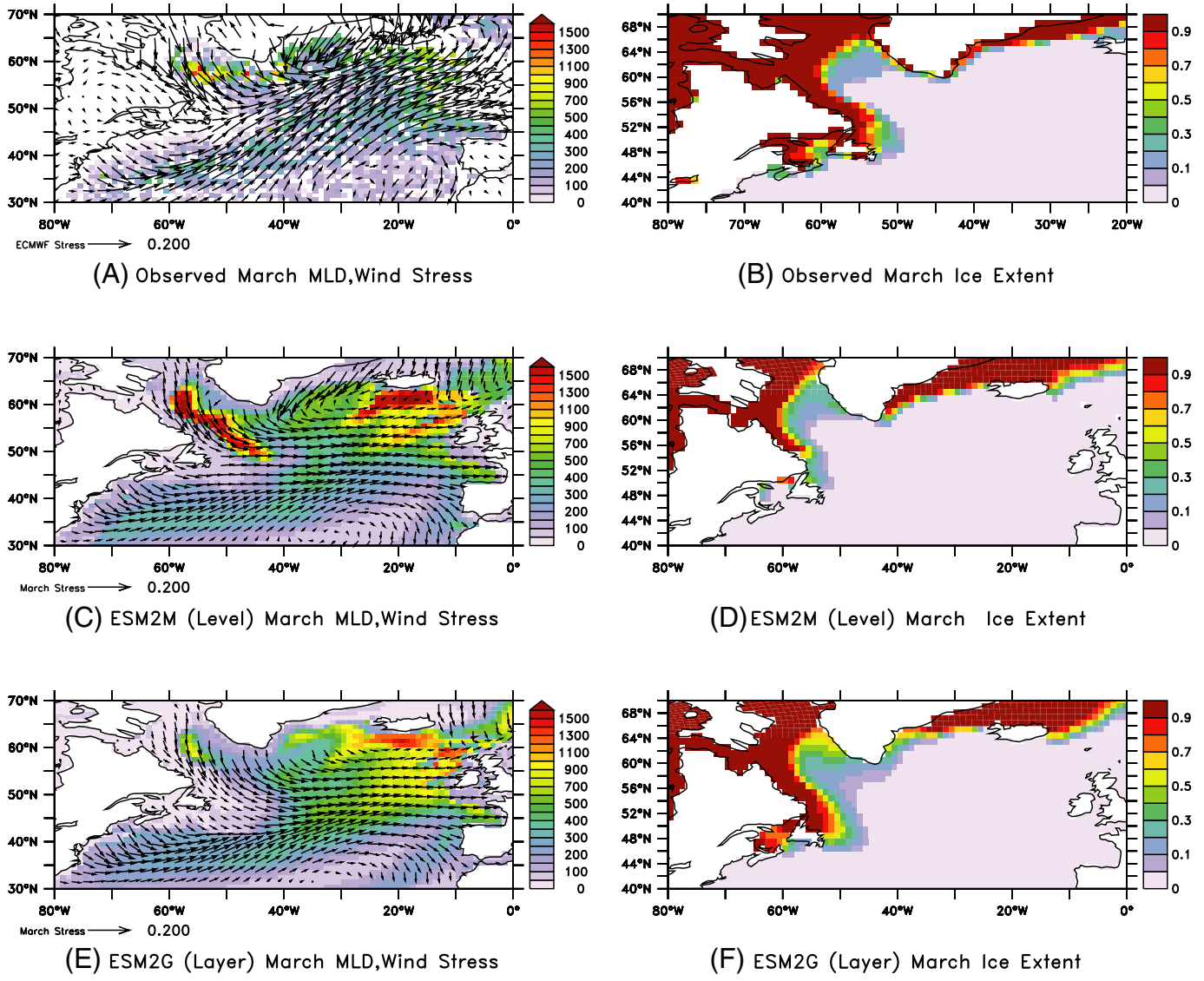

Fig. 1. Climate of the North Atlantic in March. (A) Observed mixed-layer depth from Holte et al. (2010) and ECMWF winds. (B) Observed sea ice extent (1981–2007) from an updated version of the Reynolds et al. (2002) dataset. (C) As in (A) but for level-coordinate ESM2M model, years 401–500. (D) As in (B) but for level-coordinate ESM2M model, years 401–500. (E) As in (A) but for isopycnal coordinate ESM2G model, years 401–500. (F) As in (B) but for isopycnal coordinate ESM2G model, years 401–500.

regions, though the mixed-layers still appear excessively deep relative to data in the Northeast Atlantic (Fig. 1E). Both models have trouble getting the surface southwesterly jet to extend into the Norwegian Sea. Instead, the models show this jet turning eastward near the Iceland–Scotland ridge. To the extent that the bias in winds makes it more difficult for the North Atlantic current to join up with the Norwegian Coastal Current (as the zero wind stress curl line marking the boundary between subtropical and subpolar gyres will not cross the Iceland–Scotland ridge), it may be linked to the biases in mixed-layer depth.

Fig. 1B shows the observed ice extent during the month of March defined (following Reynolds et al., 2002) as the fraction of time when ice cover exceeds the threshold of 10% detectable from microwave radiometers. A value of 1.0 within a box indicates that sea ice is always detected in that box over the period from 1981 to 2007 while values in between 0 and 1 indicate that open sea water is sometimes found at that location. During March, a patch of water where sea ice is not detected is found to the southwest of Cape Farewell and a region between 60°–64°N and 60°–50°W has intermittent sea ice. The level-coordinate ESM2M model (Fig. 1D) shows a similar pattern over years 400–500, although sea ice concentrations are generally slightly lower than observations (with reduced ice extent in the Gulf of St. Lawrence and over the Flemish Cap). The isopycnal-coordinate ESM2G model (Fig. 1F) shows more extensive ice cover than either ESM2M or the data with ice covering the entire Labrador Sea during some years. It is unclear whether the ESM2G model is biased towards allowing too extensive sea ice cover, or whether the satellite observations fail to capture past periods where sea ice has been more extensive. For example, Hill and Jones (1990) find greater ice extent off Newfoundland in the 1930s–1940s than in the 1980s.

2.2. Biogeochemical model

The ocean biogeochemical model used in both ESMs is the Tracers of Ocean Phytoplankton with Allometric Zooplankton (TOPAZ) model version 2 (Dunne, 2013). This model resolves three types of phytoplankton: small, large and diazotrophs (nitrogen fixers). Additionally, diatoms are diagnosed as a fraction of large phytoplankton. Phytoplankton growth is a function of limitation from multiple nutrients and light. Ammonia limitation is the simplest of these, and is handled using a simple Michaelis–Menten formulation, so that when it is the limiting nutrient the growth rate (μ; d^{-1})

$$\mu \propto \frac{NH_4}{K_{NH4} + NH_4}. \quad (1)$$

As described in more detail in Dunne (2013), nitrogen limitation is a combination of the simple ammonia limitation above and nitrate limitation (which is suppressed by high levels of ammonia), while phosphorus and iron limitation are handled by considering the cellular quotas of these nutrients.

Small phytoplankton tolerate lower levels of iron, phosphate, ammonia and nitrate, and the rate of grazing on them (G_S; d^{-1}) is a function of their concentration

$$G_S = \lambda_o e^{kT}(S/P_*) \quad (2)$$

where λ_0 is a grazing rate constant at 0 °C, k parameterizes a temperature-dependent increase in this grazing rate, T is the temperature in °C, S is the concentration of small phytoplankton and P_* is a scale factor at which the phytoplankton community is half S, half L. As a result, the steady-state concentration of these plankton (found by setting the growth rate in Eq. (1) equal to the grazing rate in Eq. (2)) increases linearly for very low concentrations of limiting nutrients. However, as nutrients become more abundant, a similar absolute variation in concentration results in little change in growth and thus in biomass.

Large phytoplankton, such as diatoms and green algae, require higher ambient levels of phosphorus, nitrogen and iron than small plankton (with half saturation constants three times larger), but are grazed (G_L; d^{-1}) according to the related size-dependent (allometric) parameterization from Dunne et al. (2005):

$$G_L = \lambda_o e^{kT}(L/P_*)^{1/3} \quad (3)$$

where L is the concentration of large phytoplankton and the other terms are as in Eq. (2). Thus at steady-state and very low nutrient concentrations, doubling the concentration of limiting nutrients will double the concentration of small plankton and increase the productivity by a factor of 4, but increase the concentration of large plankton by a factor of 8 and the grazing rate by a factor of 16. The great advantage of this grazing parameterization is that it requires the estimation of relatively few parameters, which can be fit from available data (Dunne et al., 2005). The fraction of the large production associated with diatoms is determined simply as the Michaelis–Menten silicate limitation term with a half saturation coefficient of 1 μmol kg^{-1}. In the North Atlantic, diatoms and non-diatoms have similar temporal behavior in our model, with diatoms dominating the large plankton biomass, although this is not the case in other basins. We therefore focus on the diatom biomass in this work. The final class represents diazotrophs which require phosphate and iron but can fix nitrogen, have low growth rates, and are grazed similarly to large phytoplankton. Diazotrophs play an important role in the nitrogen cycle, but account for a small fraction of the total primary production. We will not consider their impacts in the remainder of this paper.

As described in Dunne et al. (2012), the models are initialized from observed temperatures, salinities and nutrients and run with 1860 radiative conditions for over 1000 years. At the end of this spin-up period, drifts in both models are relatively small. The 1860 Control integrations with fixed atmospheric greenhouse gasses and aerosols start at the end of the spin-up period. Our analysis is based on the first 500 years of the 1860 Control runs.

The differences in physical forcing do result in some key differences in nutrient fields. As illustrated in Fig. 1 of Dunne et al. (2013), on a global scale, surface nitrate in the level coordinate ESM2M has a larger bias relative to data than the isopycnal coordinate ESM2G (1.6 μM vs. −0.062 μM) a larger mean error (3.6 μM vs 2.4 μM) and less well-correlated variations (r^2 of 0.87 vs. 0.91). As illustrated in Fig. 2, this carries over to the North Atlantic as well, where ESM2G shows a more realistic range in surface nitrate than ESM2M. The region where observed nitrate levels remain above the model's half-saturation constant for nitrogen uptake by diatoms (6 μM) year-round shrinks to a small region southeast of Greenland by August. ESM2G also shows nitrogen drawdown over this broad region, but the area where nutrients are retained is shifted to the northeast corner of the main basin. By contrast, ESM2M retains high nitrogen over a much larger region (Fig. 2E,F) so that a much smaller fraction of the subpolar Atlantic is nutrient limited at the end of the summer. One reason for this difference appears to be light limitation, as the depth-averaged light in the shallower mixed-layer is 20–30 W/m^2 higher in ESM2G than in ESM2M throughout the spring months in the Northwest Atlantic.

With respect to chlorophyll, the picture is more equivocal. Dunne et al. (2013) find that level-coordinate ESM2M has a higher global rms error in log chlorophyll than isopycnal coordinate ESM2G (0.31 vs. 0.28) but that it also captures the spatial pattern more accurately (r^2 of 0.54 vs 0.52). In the North Atlantic, both models fail to capture the high levels of chlorophyll seen in satellite observations, possibly a signature of overly sensitive photoadaptation. The annual-mean primary productivity in the region 80°W–0°W and 40 N–65°N is 2.7 mol/m^2 in ESM2M and 2.1 mol/m^2 in ESM2G both of which lie within the range of satellite-based estimates reported in Dunne et al. (2007) which range from 1.9 to 3.5 mol/m^2 with a mean of 2.7 mol/m^2.

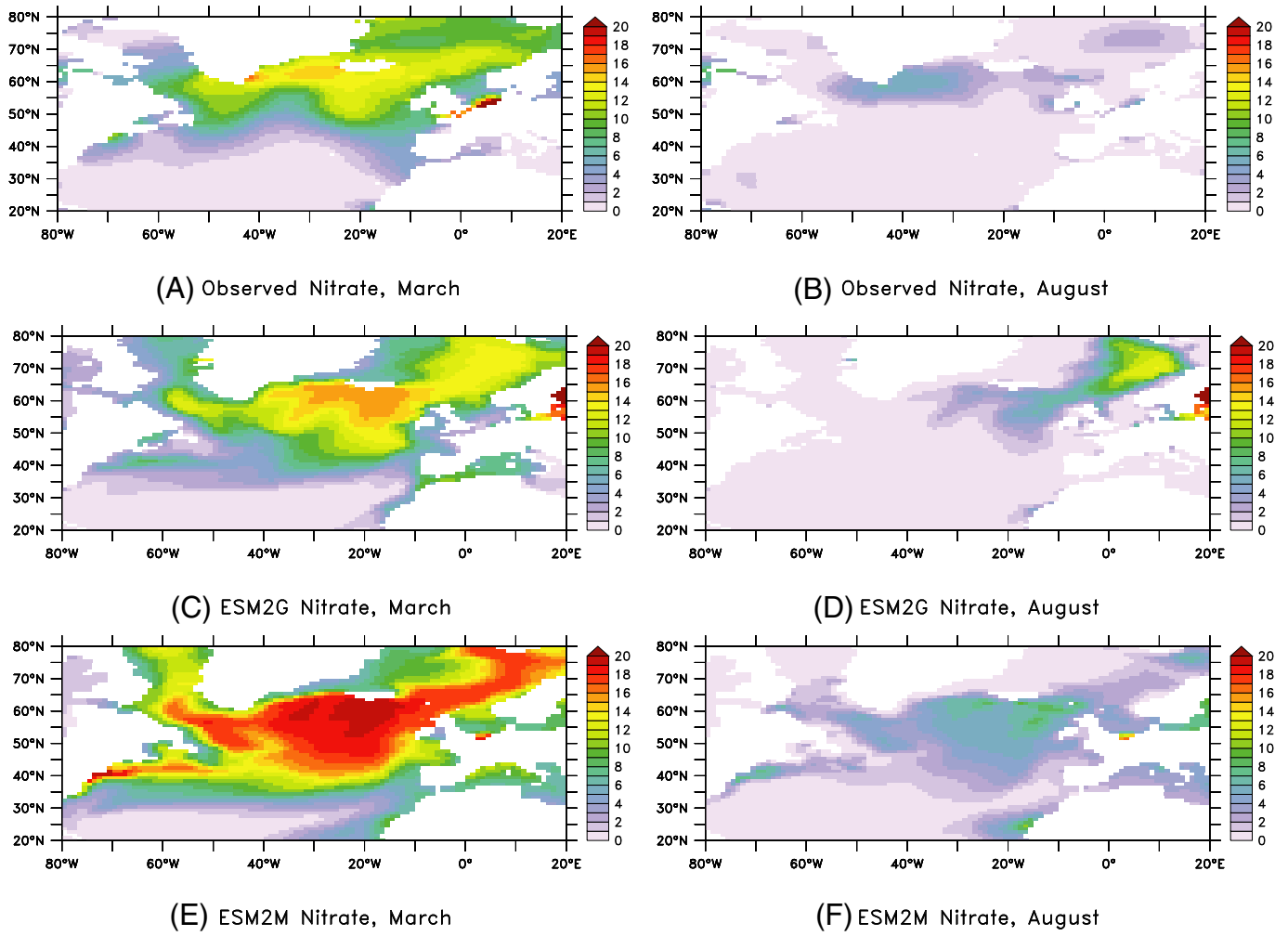

Fig. 2. Nitrate concentrations in mmol m^{-3} in the North Atlantic. Observations are from the World Ocean Atlas 2005 (Garcia et al., 2006). Models are results averaged over years 1–500 of the 1860 Control Run. (A) Observations, March. (B) Observations, August. (C) ESM2G, March. (D) ESM2G, August. (E) ESM2M March. (F) ESM2M, August.

3. Atlantic temperature variability in the two models

We begin by examining 600-year time series of the AMO index in ESM2M and ESM2G (Fig. 3A). Both models show significant variability at interdecadal time scales, though the amplitude of the variability is significantly larger in ESM2G (standard deviation of 0.15 °C) than ESM2M (standard deviation of 0.075 °C). ESM2G also shows much more skewed variability towards intense cold periods. The 10 year autocorrelation of the AMO index in ESM2G is 0.44, implying only about 19 degrees of freedom, so that correlations with a magnitude greater than 0.44 are significant at the 95% confidence level. By contrast, the 10-year autocorrelation is only 0.21 for ESM2M, implying about 32 degrees of freedom so that correlations with a magnitude greater than 0.35 are significant at the 95% confidence level.

Regressing the AMO index onto the decadally smoothed SSTs (Fig. 3B,C) shows that the most intense temperature signals in both models are concentrated in the Northwest Atlantic and Labrador Sea as well in the Norwegian Sea in ESM2M with a change of 1 °C over the entire basin corresponding to changes in excess of 4 °C over large swathes of these regions. Both models also show similar patterns of changes south of 45°N, with a cold anomaly off of North America and two tongues of warm anomalies emanating into the subtropical gyres. Local differences between these patterns likely arise from different representations of the path of the North Atlantic Current. In both models a 1 °C change in basin-mean temperature corresponds to a significantly smaller warming at low latitudes. The concentration of the highest regressions in the Northwest Atlantic is common to many climate models (Ting et al., 2011). It should be noted that as one progresses to longer and longer temporal averages (corresponding to periods more characteristic of the data than of most climate models) the warming signal becomes more uniform over the basin. Observational estimates of AMO variability reported in Ting et al. (2011) show a pattern that is consistent with such longer temporal averages, though it is unclear how much of this is due to undersampling of the convective regions in the Northwest Atlantic. By contrast, Stein (2007) finds a much larger signal in the Northwest Atlantic, both using in-situ temperatures at Greenland and the NOAA extended SST reconstruction. Regressing the AMO index vs. SSS (Fig. 3D,E) shows that in addition to the signal in temperature, there is also a strong signal in salinity in the subpolar gyre, with warmer temperatures corresponding to higher salinities. As with temperature, this signal is concentrated in the Labrador Sea, but also propagates out into the main Atlantic basin.

Regression coefficients for salinity are about half those for temperature, so that a 0.5 °C change in AMO index results in a peak change in annual mean SST of about 2.5 °C and a peak change in SSS of ~1 PSU. At the low temperatures found in the subpolar Atlantic, this implies that a higher AMO index is associated with denser surface waters in the Northwest Atlantic. One would thus expect that a high AMO index

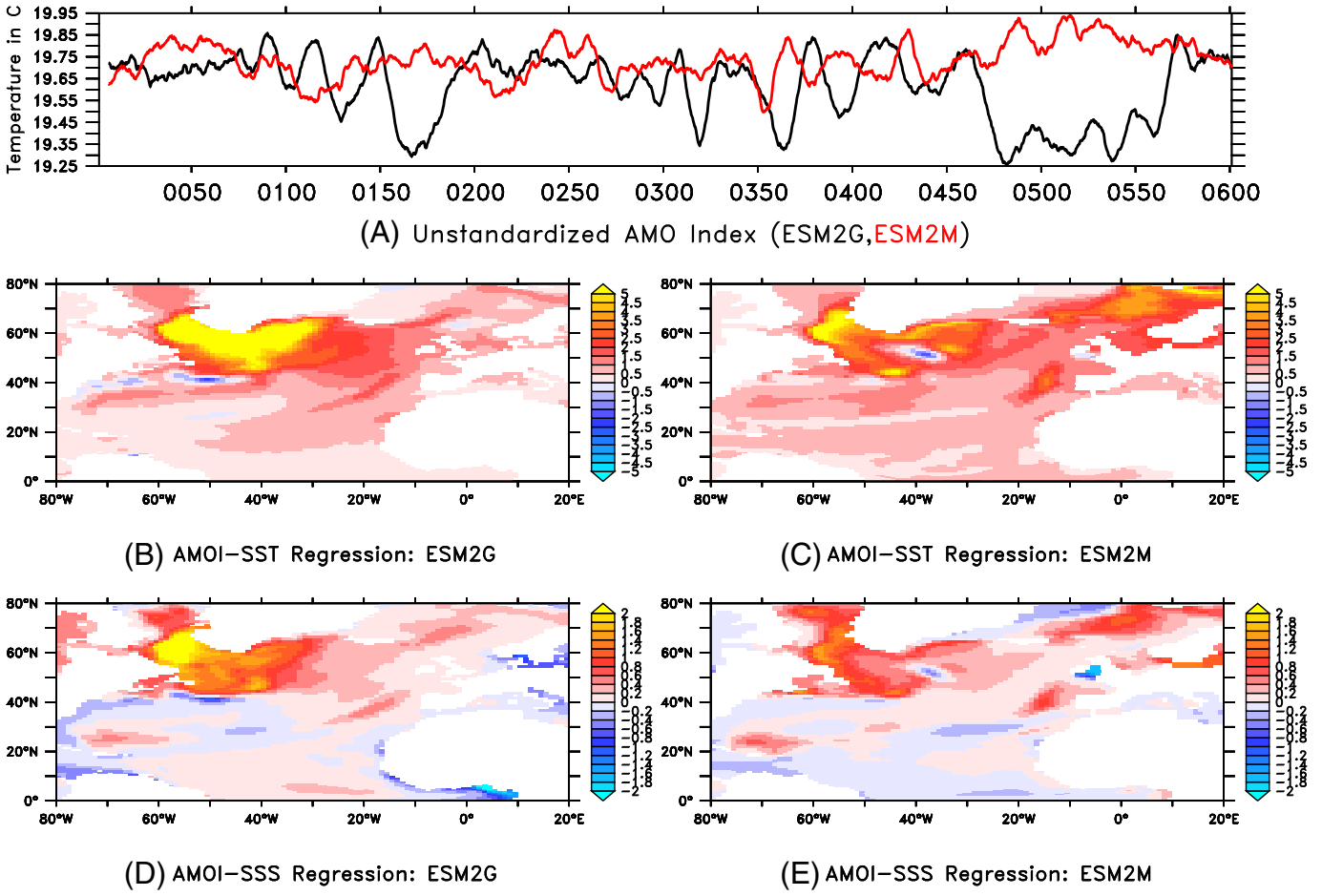

Fig. 3. Atlantic temperature variability in ESM2M and ESM2G. (A) Unstandardized AMO index (averaged SST between equator and 70°N in the Atlantic basin, decadally smoothed). (B) Regression coefficient between the decadally smoothed local SST and the AMO index (°C/°C) for ESM2G. A value of 2 means that the local SST change is twice the AMO index. (C) Same as (B) for ESM2M. (D) Regression coefficient between the decadally smoothed SSS and the AMO index (PSU/°C) for ESM2G. A value of 2 means that a 1 °C change in the AMO index would correspond to a 2PSU change in surface salinity. (E) Same as (D) but for ESM2M.

would be associated with deeper mixing. Fig. 4 shows the correlation between AMO index and the decadally smoothed log of the mixed-layer depth during March (Fig. 4A and C) and August (Fig. 4B and D) for the two models. In both models, a warmer Atlantic is correlated with deeper wintertime mixed-layers throughout the Northwest Atlantic, but with a notably different pattern during the summer months. The spatial extent of enhanced wintertime mixing is much greater in ESM2G than in ESM2M.

The relationship between the AMO index and salinity in Fig. 3 and mixed-layer depth in Fig. 4 suggests a possible connection with the thermohaline circulation. While such a connection does exist in both ESM2M and ESM2G, it is expressed quite differently in the two models. As shown in Fig. 5A the relationship between the standardized AMO index (anomaly divided by the standard deviation) and standardized overturning anomalies is quite good in ESM2G. Overturning anomalies computed in density space at 26°N and 45°N show an obvious relationship with the AMO index, and a lag correlation (solid lines, Fig. 5C) shows the overturning at 45°N leading the AMO by about 4 years and the overturning at 26°N leading by about 2 years. Peak correlations are very high, exceeding 0.9 for the overturning at 45°N. The phase relationship is consistent with an increasing in the overturning driving warming of the Atlantic. By contrast, the relationship between AMO index and overturning in ESM2M is much weaker with correlations peaking only at a level of 0.5 or so (though it should be noted that this is still highly significant). The overturning in ESM2M does exhibit a similar phase relationship to the AMO index as in ESM2G.

The differences between the models can also be seen in the spectra of the standardized AMO index and overturning anomalies (Fig. 5D). Not surprisingly given the high correlation between the overturning and AMO index, ESM2G shows consistent spectra between the three time series, with a broad peak at periods between 20 and 90 years. ESM2M shows rather different spectra for the AMO index (which has a peak at lower frequencies) and the overturning (with a relatively strong peak at around 20–30 years period).

A connection between Atlantic temperatures and overturning is not surprising, given the extensive literature on how disruption of the AMOC by freshwater pulses can cool the North Atlantic (Stouffer et al., 2006 demonstrates this for a range of models). While the mechanism for such a cooling has been disputed it is likely some combination of a weaker overturning physically transporting a smaller volume of warmer surface waters into this region, shallower wintertime convection bringing up less heat and allowing more formation of sea ice during the wintertime, with radiative feedbacks enhancing these effects (Herweijer et al., 2005).

While a complete analysis of the feedbacks responsible for the difference in overturning behavior in the two models is beyond the scope of this paper, we can make some preliminary statements about mechanisms that may contribute to the differences. If one thinks of the overturning as a pressure-driven oceanic circulation, the key question that arises is why the driving pressure gradients vary. The fact that the overturning is associated with saltier, warmer waters in high latitudes suggests that one focus should be explaining changes in the

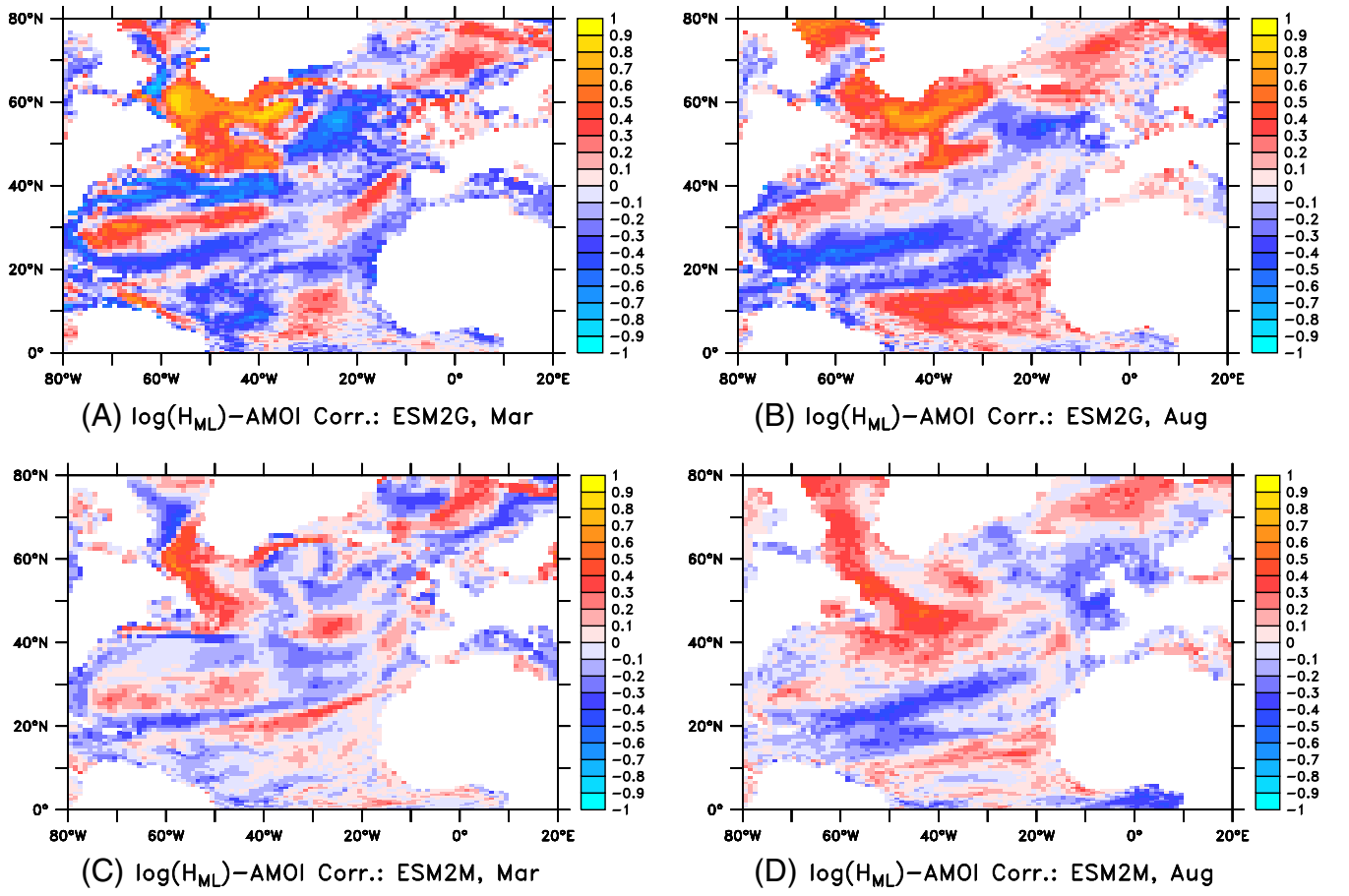

Fig. 4. Correlation between the AMO index and log of the mixed-layer depth in ESM control runs. (A) March, ESM2G. (B) August, ESM2G. (C) March, ESM2M. (D) August, ESM2M.

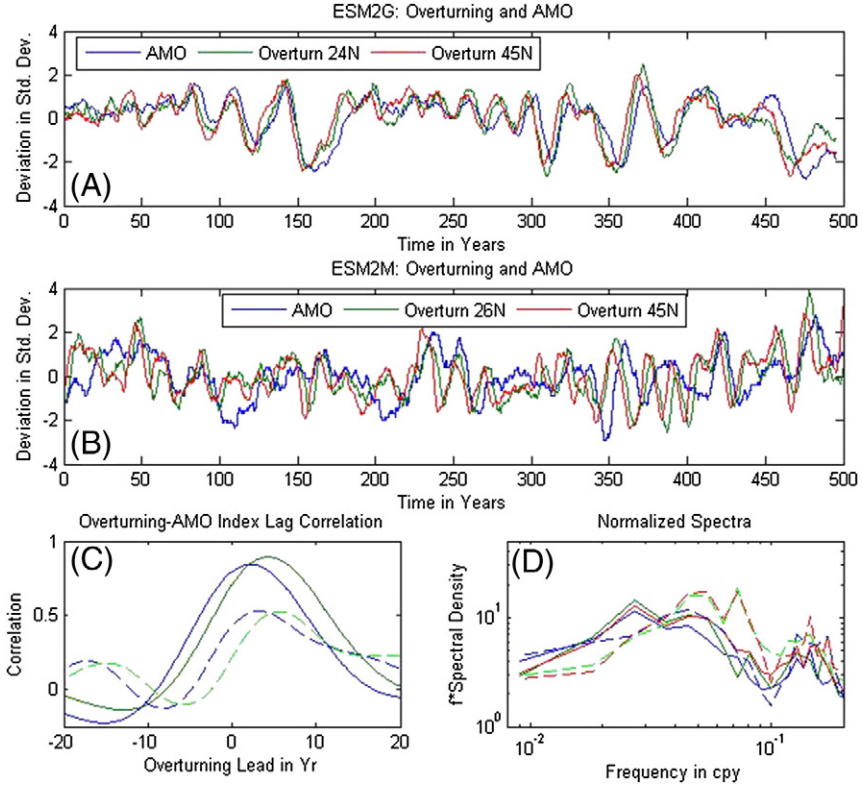

Fig. 5. Relationship between the AMO index and density-space overturning in the two ESMs. (A) and (B) show standardized anomalies of AMO index and overturning in density space at 45°N and 26°N for the first 600 years of the 1860 Control Run. (C) Lagged correlations between AMO index and overturning with overturning lead in years. (D) Spectra of overturning and AMO index. Horizontal axis is in cycles per year (cpy). Solid lines in (C) and (D) are ESM2G, dashed lines ESM2M.

salinity on decadal time scales. Examining the correlations between decadally smoothed overturning and net surface freshwater flux in the two models (colors in Fig. 6A,C), we see that higher overturning is correlated with excess evaporation over the center of the subpolar gyre and excess precipitation/ice melt/runoff along in the vicinity of the boundary currents in both models. The correlations are much higher in ESM2G than in ESM2M. In both models, hydrological feedbacks would seem to enhance surface salinity anomalies in the convective regions. In ESM2G, a 1 Sv increase in overturning is associated with a 70 mm/yr decline in freshwater flux over region 50°W–40°W and 45°–55°N with a highly significant ($p < 0.0035$) correlation coefficient of −0.57. Such a change represents a substantial fraction of the 511 mm yr^{-1} of net freshwater added to the ocean annually in this region by both precipitation and runoff. Over the course of a decade, an anomalous flux of this size would change the salinity of the top 100 m of the ocean by 0.25 PSU. In ESM2M the same region has a correlation coefficient of −0.21 (which is just short of being significant at the 90% confidence level), and a 1 Sv increase in overturning is associated with a much smaller −16 mm yr^{-1} change in freshwater flux.

Annual mean wind stresses in both models show high overturning to be connected with stronger winds out of the Arctic, but in ESM2G this flow is connected with a more intense anticyclonic flow off Greenland (consistent with a westward movement of the Icelandic low), whereas in ESM2M the connection extends out towards Europe. This means that in ESM2G, a high overturning is associated with much stronger Ekman upwelling of salty warm deep water in the Northwest Atlantic than in ESM2M, potentially adding a second mechanism for reinforcing surface salinity anomalies.

If we ask how such salinity anomalies would become established in the first place, we get a slightly different picture. Correlating annual mean freshwater and momentum fluxes with changes in the overturning (Fig. 6B,D) we see that the correlation between the net water flux and the annual overturning trend (in Sv/yr) is much smaller than it is for the overturning. Moreover, it is also of the wrong sign over much of the Northwest Atlantic, with increasing overturning associated with more water entering the ocean (a similar picture emerges in ESM2G if one simply uses the salinity from 40°–50°W and 45°–55°N). Increasing overturning in both models is associated with a cyclonic atmosphere circulation south of Iceland. This is broadly consistent with recently published work by Hakkinen et al. (2011) who related the AMO index to changes in the 2nd PC of SLP, which has a similar center of action to what we see in both ESM2M and ESM2G. Comparison of their Figs. 1B and 2B show that when the detrended AMO index is increasing (1920, 1990s) there is a positive wind stress curl anomaly over this region, whereas the decrease in the same index in the late 1950s and 1960s is associated with lower wind stress curl. In ESM2G the anomalous cyclonic circulation is stronger and extends further to the south than in ESM2M. Insofar as decadal salinity anomalies are important drivers of overturning variability, the suggestion from Fig. 6 is that the two models differ in relatively subtle ways in how such salinity anomalies are generated by winds over the North Atlantic and how effective atmospheric feedbacks are at maintaining them.

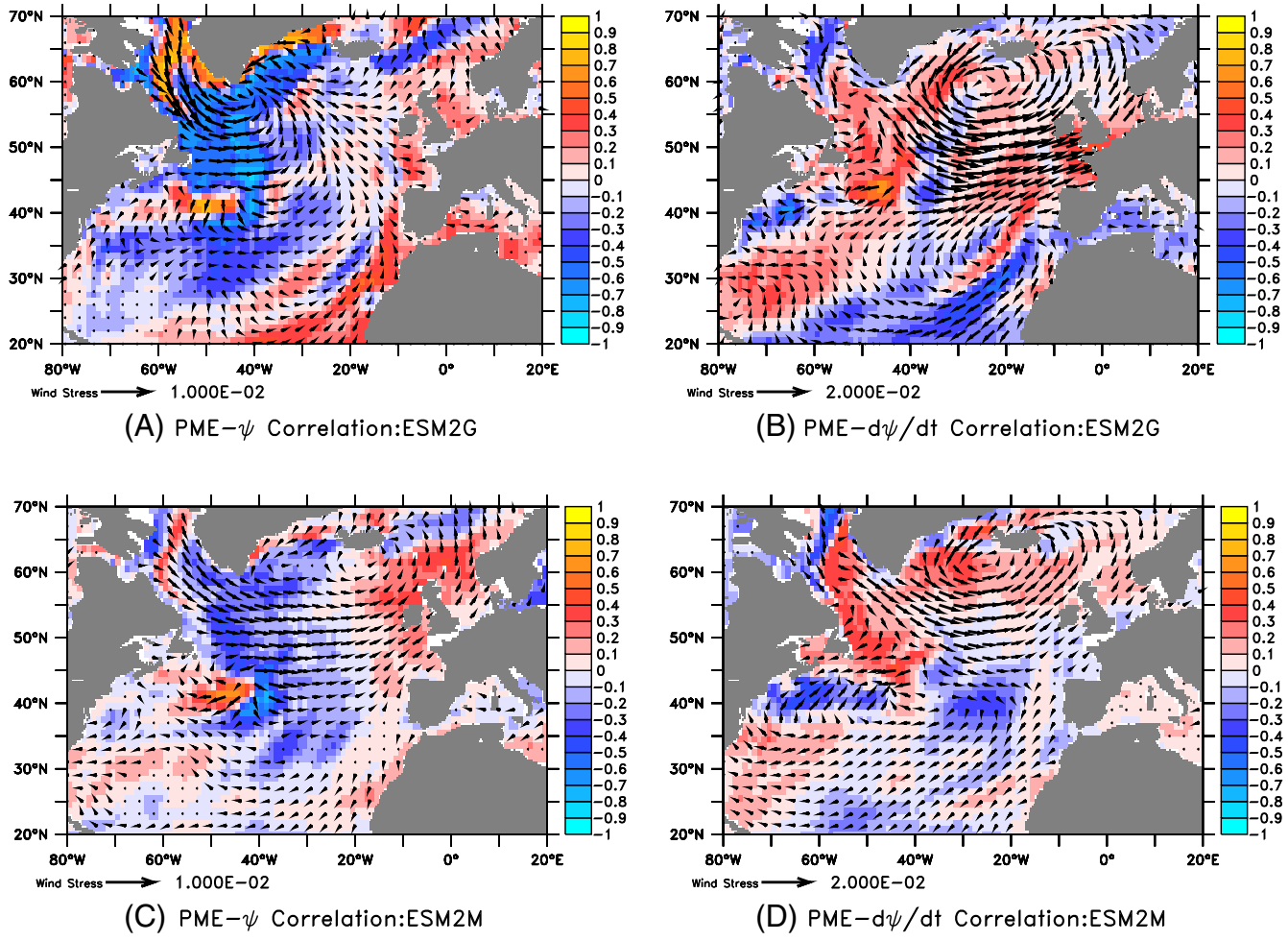

Fig. 6. Correlation between overturning streamfunction (left column) and its change (right column) and precipitation minus evaporation (colors) and wind stress (vectors). Top row shows results for ESM2G, bottom row for ESM2M.

4. Relationship between AMO index and biological variability

Using output from GFDL's prototype ESM2.1, Gnanadesikan et al. (2011) showed that the variability in the biomass of large phytoplankton was much more extreme than total phytoplankton biomass, both in the annual mean and by seasons. The reason for this is clear from Eq. (2). In order for grazing to match similar relative changes in phytoplankton growth rate, much larger changes are required for large phytoplankton biomass than for small phytoplankton biomass. Fig. 7A shows the coefficient of variability for decadal variation in diatom biomass in ESM2G (colors) and ESM2M (contours) respectively. A striking result is how little variability there is in annual-mean biomass (Fig. 7A) over the majority of the subpolar North Atlantic, with coefficients of variation in both models less than 0.1. The exception in ESM2G is in the northwest Labrador Sea and off of Norway. This lack of interannual variation is also consistent with recent work by Henson et al. (2009) examining the interannual variability in satellite-estimated primary productivity.

However, when we examine the coefficient of variation of decadally smoothed biomass in each month, much larger variations are seen. Fig. 7B–D shows the coefficient of variation for diatom biomass decadally smoothed over April, July and October respectively. Large coefficients of variation are seen throughout the basin in April in both models, with the highest values in the Labrador and Norwegian Seas. In July and September ESM2M shows higher variability at low latitudes. By contrast ESM2G shows most variability at high latitudes with values greater than 0.4 seen in the Labrador Sea, off Norway and at the edge of the Bay of Biscay shelf.

We can examine which of these regions shows the highest correlation with the meridional overturning circulation by performing a composite analysis in which we examine the differences between those times when the overturning circulation or AMO index is more than one standard deviation above its mean and those times when the corresponding index is more than one standard deviation below its mean (note that because of the lag between the overturning and AMO index, these composites will correspond to slightly different years). Composites for ESM2G are shown in Fig. 8 with colors showing the log of the ratio of large diatom biomass between high and low AMO Index periods and contours showing the difference in nitrate concentration during April, June, August and October. A clear pattern emerges during the summer months whereby nitrate concentrations are higher in the Labrador Sea and lower in the eastern Atlantic, and diatom biomass ratios follow this general pattern. The pattern of nitrate change mimics the pattern of mixed-layer depth changes in Fig. 4 throughout subpolar latitudes. Note that the variability off of Norway is relatively unrelated to the AMO Index. Analysis of what drives this variability shows it to be related to the summertime depth of the transition layer. Essentially, times with low biomass correspond to times with shallow mixed-layers, but very deep transition layers, so that each day's production is rapidly mixed below the euphotic zone. Given the likelihood that the signal off Norway in ESM2G is a numerical artifact of the lack of resolution below the mixed-layer, we will not discuss it further in this paper.

The analogous picture for ESM2M (Fig. 9) shows similar patterns of nutrient variability (higher nutrients in the Northwest Atlantic, lower in the Northeast under warm conditions), but the amplitude of variability

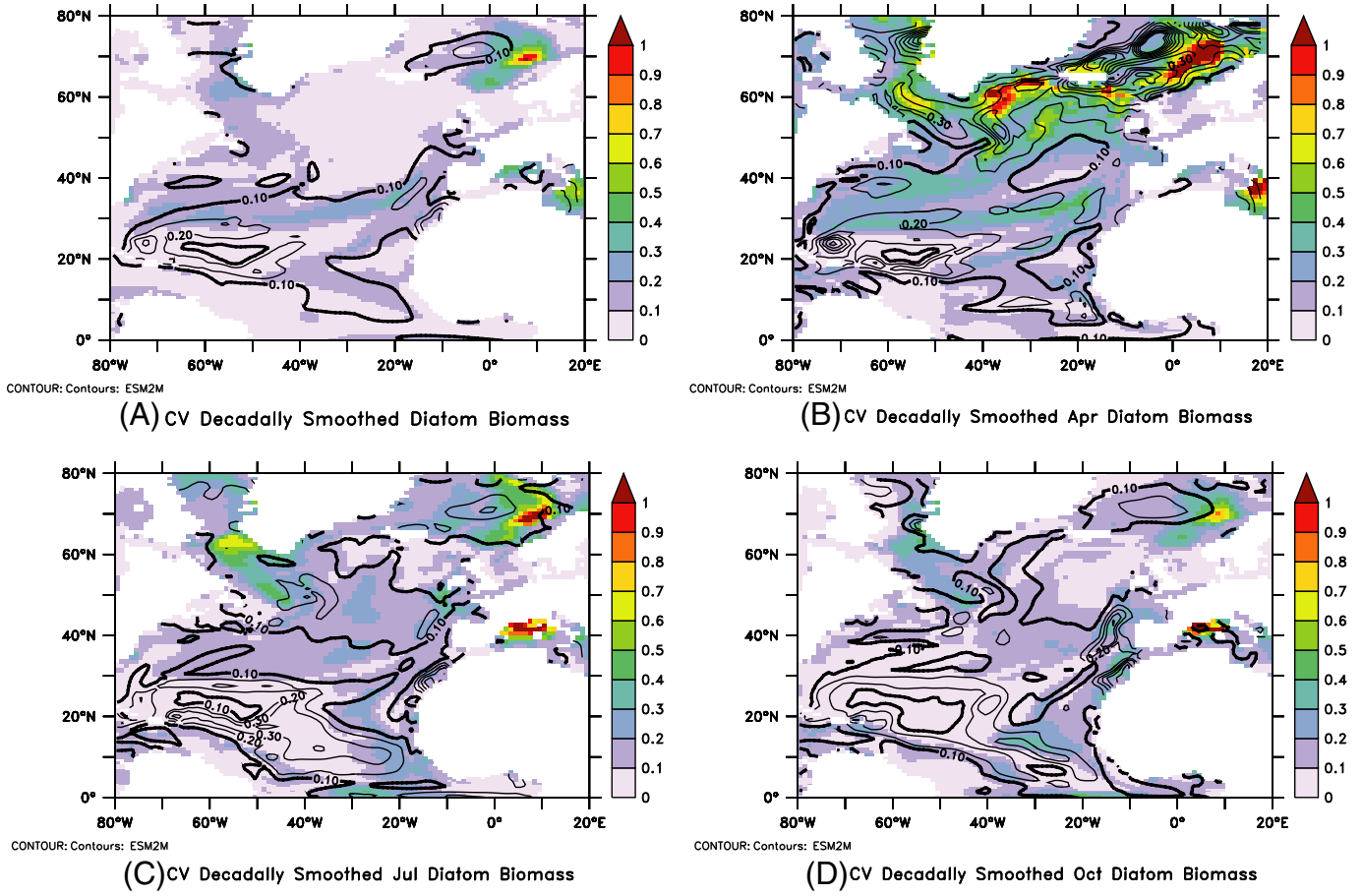

Fig. 7. Coefficient of variability (standard deviation/mean) of decadally smoothed diatom biomass. Colors are for ESM2G, contours for ESM2M. (A) Decadally smoothed diatom biomass. (B) Decadally smoothed April biomass. (C) Decadally smoothed July biomass. (D) Decadally smoothed October biomass.

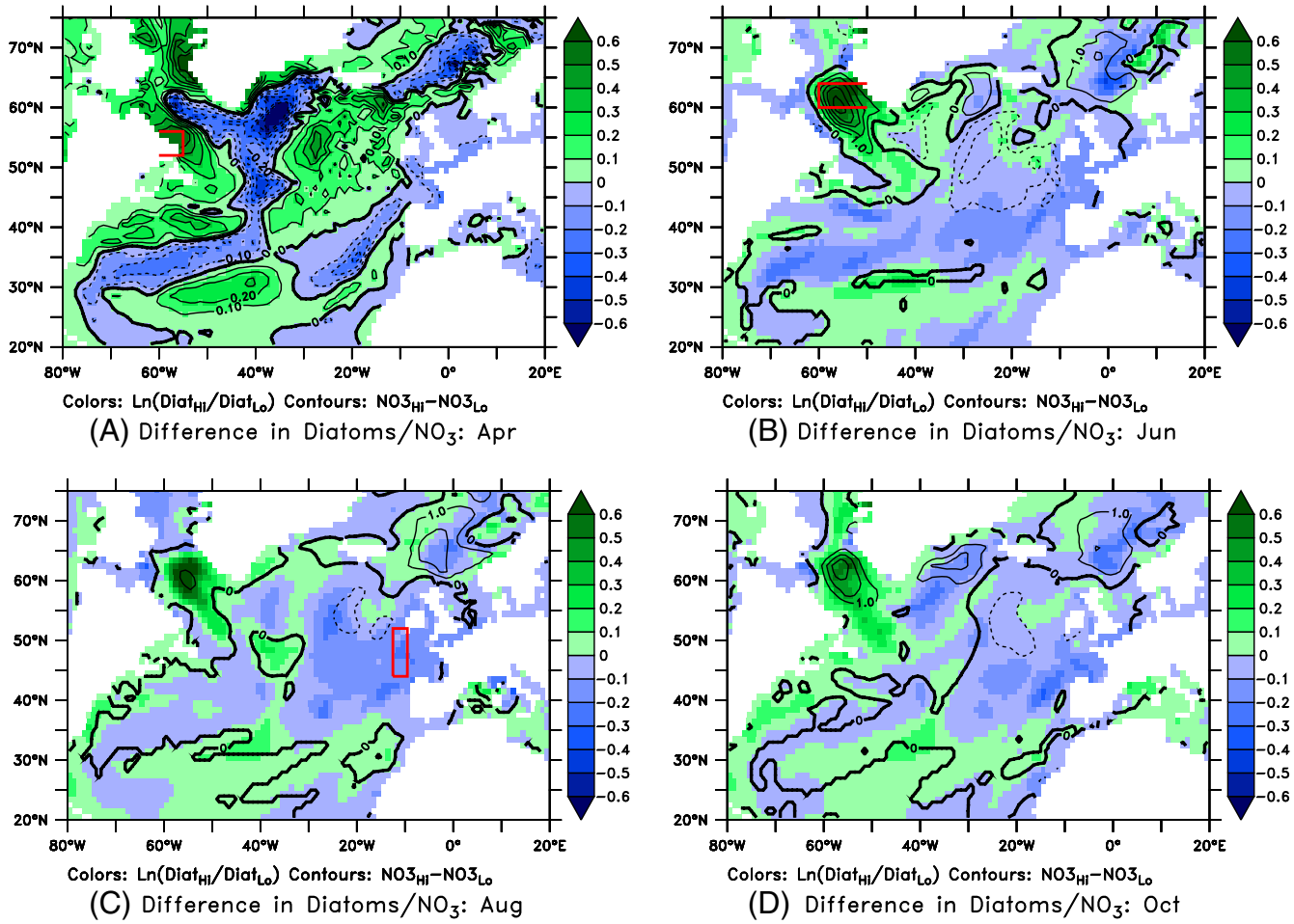

Fig. 8. Composites of the difference in diatom biomass and surface nutrients between high AMO index years and low AMO index years for the ESM2G model. Colors show natural log of the ratio in diatom biomass, contours show the difference in dissolved nitrate in mmol m^{-3}. Red boxes denote regions analyzed in the text. (A) April, (B) June, (C) August and (D) October.

is far smaller (1–2 μM rather than more than 6 μM). ESM2M exhibits much less variability in diatom biomass. Larger variability in diatom biomass in ESM2M relative to ESM2G is seen in April in the Greenland Sea, near a region which also sees higher variability in temperature and mixed-layer depth.

The heterogeneity in diatom biomass variability seen across the basin and between the different models demonstrates that a simplistic view of how biomass and temperature are linked is unlikely to work. In the three subsections that follow we discuss three different regions where significant interdecadal variability in biomass is linked to the basin-mean SST. We choose these regions based upon the limiting factors for the diatom biomass and the physics involved in setting those limits. The regions are chosen to be illustrative of how significant changes in phenology can be linked to the AMO and AMOC rather than being an exhaustive catalog of all possible relationships. Because ESM2M shows so little variability we focus on ESM2G.

4.1. Nutrient-limited, convectively supplied (Labrador Sea)

We begin by looking at an area to the west of Greenland, stretching across longitudes 50°–60°W and latitudes 60°–64°N shown by the red box in Fig. 8B. As shown in Fig. 8, in ESM2G the diatom biomass is much higher in this region from April through August during warm periods than during cold periods, and nutrients are higher as well. A composite of the annual cycle of diatom biomass in this region during warm and cold periods (Fig. 10A) shows that the biomass peaks later and persists longer under warm periods (solid green lines) than under cold periods (solid blue lines). The relationship is similar when the overturning in density space at 45°N is used to segregate different periods (dashed lines). We can isolate the relevant mechanism driving these differences by looking at the ratio of various fields under the different regimes. As seen in Fig. 10B, the high AMO/overturning regime off of Greenland is associated with lower diatom biomass (green lines) and higher mixed-layer depth (black lines), light (blue lines) and nutrients (magenta lines) during the winter months. During the summer, light and mixed-layer depths are essentially the same for high and low AMO index and overturning, but high nutrients persist through the summer and result in higher levels of diatom biomass throughout the summer months.

The relationships suggested by the composite analysis can also be seen by looking at scatterplots between summertime diatom biomass and other fields over time (Fig. 11). Fig. 11A shows the relationship between diatom biomass in June averaged over the West Greenland area and mean mixed-layer depth in the previous March, when mixed-layers in this region are at their deepest. The correlation between the two is 0.76 without decadal smoothing and 0.89 with it (much larger than the 0.44 we used as the 95% significance level for correlation with AMO in this model). Note that the diatom biomass during June ranges over a factor of 5. By contrast, the correlation between June mixed-layer depth and diatom biomass is much weaker. Without decadal smoothing the correlation coefficient of 0.13 is insignificant ($p < 0.28$) and it reaches 0.43($p < 0.025$) with decadal smoothing. There is clearly a strong relationship between June biomass and June nitrate (red points, Fig. 11B) with a correlation coefficient of 0.97. Given

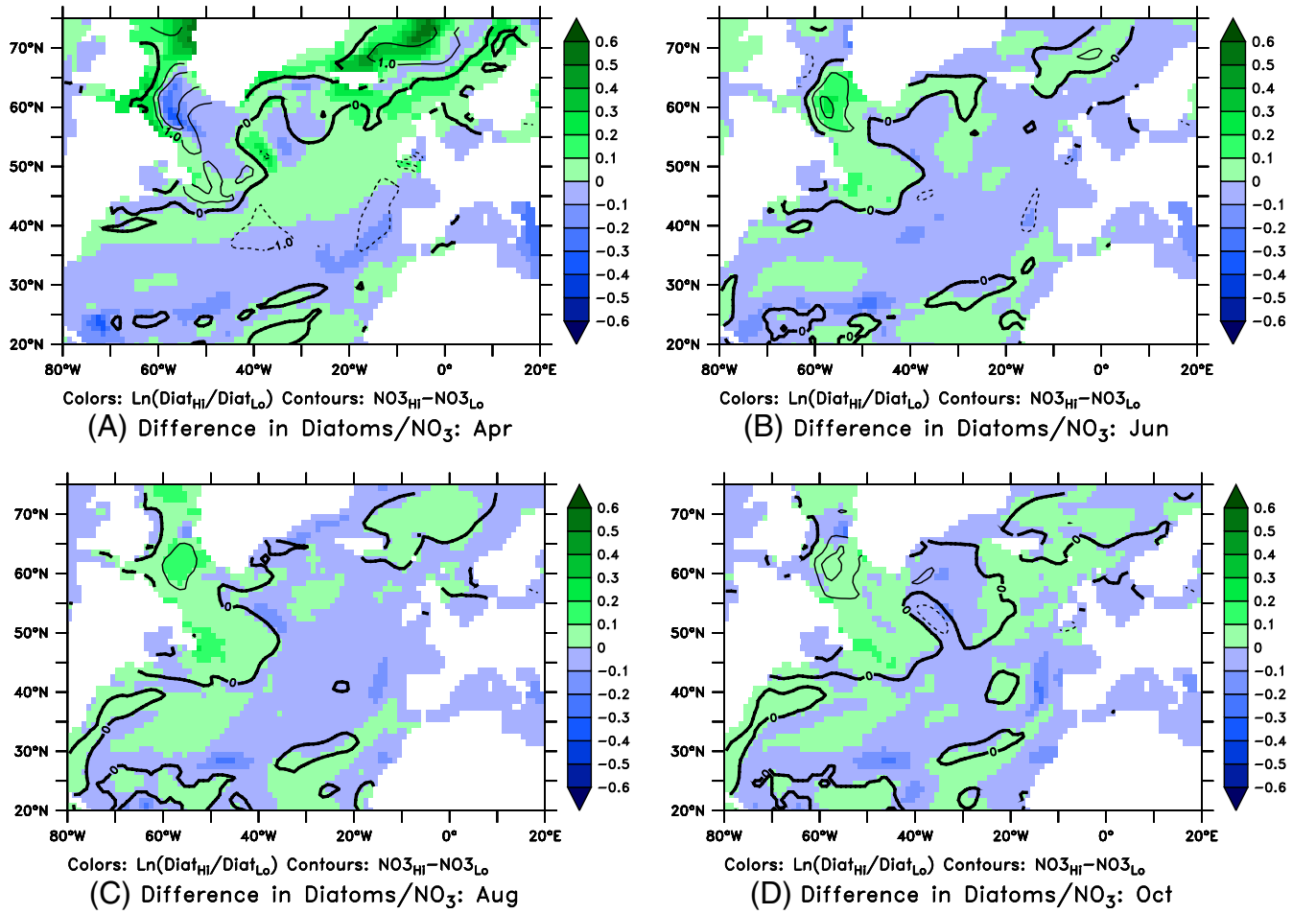

Fig. 9. Composites of the difference in diatom biomass and surface nutrients between high AMO index years and low AMO index years for the ESM2M model. Colors show natural log of the ratio in diatom biomass, contours show the difference in dissolved nitrate in mmol m^{-3}. (A) April, (B) June, (C) August, and (D) October.

that the nitrate concentrations are varying across the range where limitation is expected to occur, this correlation is not surprising. The approximately 5 μM range in June nitrate is mirrored by a similar range in concentrations during March (black points, Fig. 11B) with a correlation between June nitrate concentration and March nitrate concentration of 0.88.

Plotting the diatom biomass vs. the standardized overturning anomaly and standardized AMO index (Fig. 11C), we see a tighter relationship between the overturning and the diatom biomass (with a lag-0 correlation of 0.82) than with the AMO index (0.71). In fact, the diatom biomass leads the AMO index by about 4 years (with a maximum correlation of 0.83), similar to the overturning. The lagged correlation analysis thus suggests that the relationship between diatom biomass and temperature in this region is actually secondary to the relationship with convection and overturning.

Finally, looking at the surface salinity (black points, Fig. 10D) and 200 m salinity (red points Fig. 10D), we see that the variability in biomass is clearly related to salinity stratification. Time periods with high biomass are marked with high wintertime surface salinities, matching those at 200 m, which vary relatively little. We note that the range in surface salinities of ~1.0 PSU (with most of the points lying between 33.6 and 34.4) is actually quite consistent with the shorter time series reported in Belkin et al. (1998) in the West Greenland Current. The changes in surface salinity are very tightly linked to changes in average salinity over the top 200 m (with a correlation coefficient of 0.99 and a regression coefficient of 0.64), so the surface anomalies are not simply the result of changes in mixing. However, it is also the case in ESM2G that warm periods are associated with higher winds and wind stress, and cold periods with lower winds and wind stress—possibly resulting in a positive feedback. Low stratification and higher winds result in turbulence bringing up warm water and nutrients. In ESM2G, this results in alleviation of nutrient limitation during the summer months and allows for much higher biomass. In ESM2M, by contrast, nutrients stay high during the summer months and any variability in diatom biomass is driven by changes in mixed-layer depths which have a much weaker relationship with the AMO index (Fig. 4).

4.2. Ice edge regime (55°–60°W, 52°–56°N)

Higher overturning is associated with more import of warm water into high latitudes. This can result in an earlier melt-back of sea ice during the spring, relieving light limitation on the mixed-layer and producing an earlier spring bloom. This effect shows up particularly strongly off the northern coast of Labrador in ESM2G shown by the red box in Fig. 8A. As shown in Fig. 10C, in this region high AMO index/overturning is associated with higher biomass and an earlier spring bloom. Plotting April diatom biomass vs. nitrate (Fig. 12A) shows some relationship (the correlation coefficient of 0.53 has a probability <0.007 of occurring by chance), but the range in biomass is far larger in a relative sense than the range in nutrients, which are at levels at which nitrate is only mildly

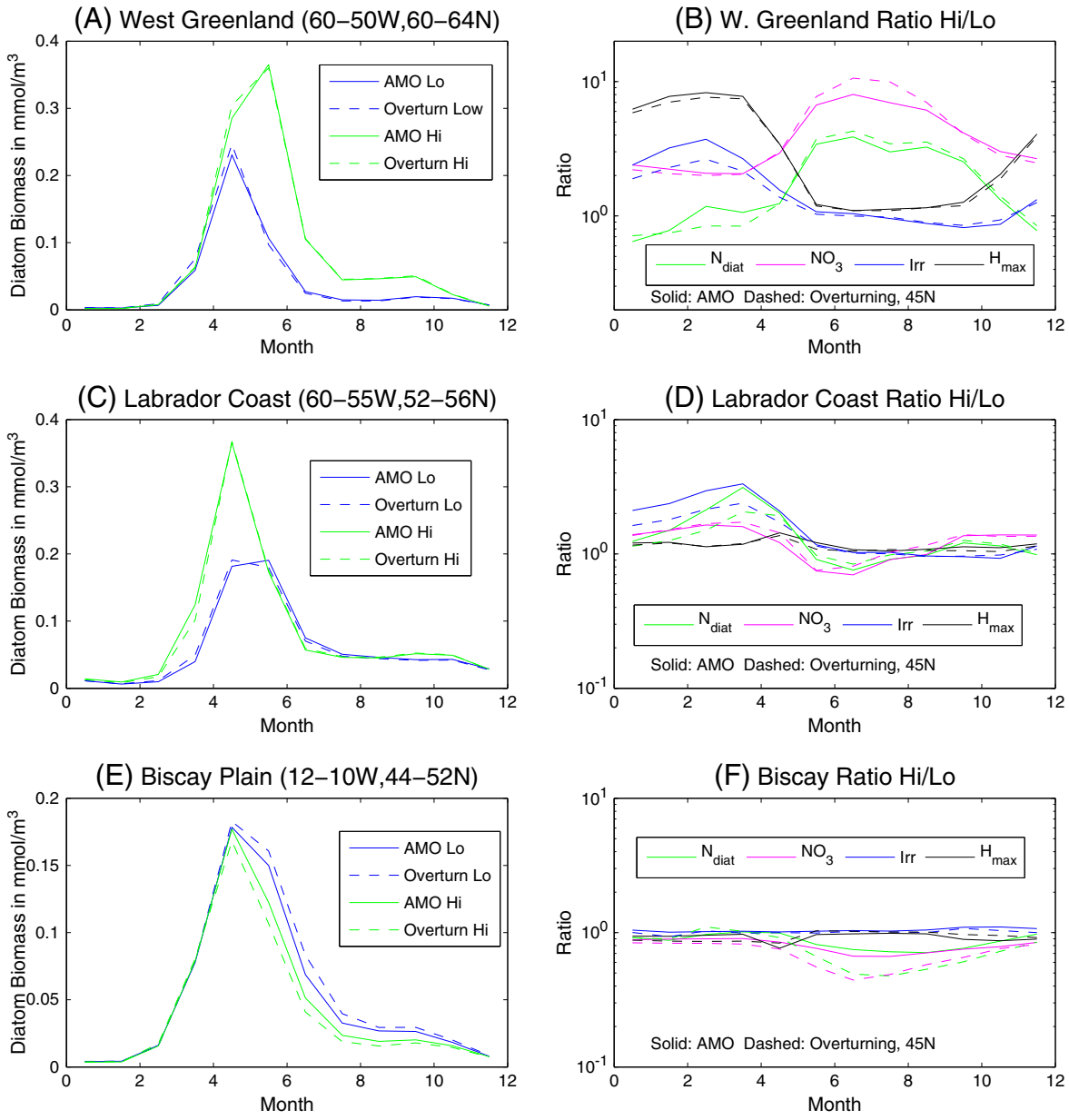

Fig. 10. Composite seasonal cycle in three locations that show linkages between the AMO index/overturning in density space and diatom biomass in ESM2G. Left column shows diatom biomass under low AMO/overturning (blue lines) and high AMO/overturning (green lines). Right column shows the ratio of various quantities between high and low periods, solid lines when the AMO is used to discriminate, dashed lines with the overturning at 45°N is used. Green lines show changes in diatom biomass, magenta lines, nitrate, blue lines mixed layer irradiance and black lines mixed layer depth. Top row: West Greenland. Middle row: Labrador Coast. Bottom Row: Bay of Biscay shelfbreak.

limiting. By contrast, the relationship between biomass and light is much tighter (Fig. 12B), with the sevenfold range in biomass corresponding to a comparable range in light and a correlation coefficient of 0.94. The variation in light levels can largely be explained by variations in ice extent (Fig. 12C), which are anticorrelated with April diatom biomass (−0.94).

Comparing the AMO index (solid) and overturning (dashed) curves in Fig. 9D, one notices a more extreme response in the former. In contrast to the previous region considered, the correlation between spring biomass off the Labrador coast is better correlated with the AMO index (0.82) than with the overturning at 45°N (0.64, $p < 0.0012$). When the overturning leads the spring diatom biomass by 4–6 years the correlation rises to around 0.80. The scenario suggested by these analyses is one where an increase in overturning leads to a warming of the Northwest Atlantic, melting back sea ice during the spring and leading to an earlier spring bloom. Conversely, a decrease in overturning leads to less heat being brought to the surface in the winter, more sea-ice cover and light limitation during the spring and a later spring bloom.

4.3. Nutrient-limited advective supply (Biscay Plain, 10° – 12°W,44° – 52°N)

A final region which shows a strong relationship with the overturning is Northeast Atlantic off the continental shelves of France and Ireland shown by the red box in Fig. 8C. While we chose this region because it shows strong variability in the fall bloom, observations also show strong blooms along the shelf edge (Garcia-Soto and Pingree, 2009). In this region, warm/high overturning conditions are found to give lower diatom biomass (Fig. 10E,F) and surface nitrate (Fig. 10F). Light and mixed-layer depths appear to have a relatively minor impact on the growth rates. The diatom biomass varies much more when overturning

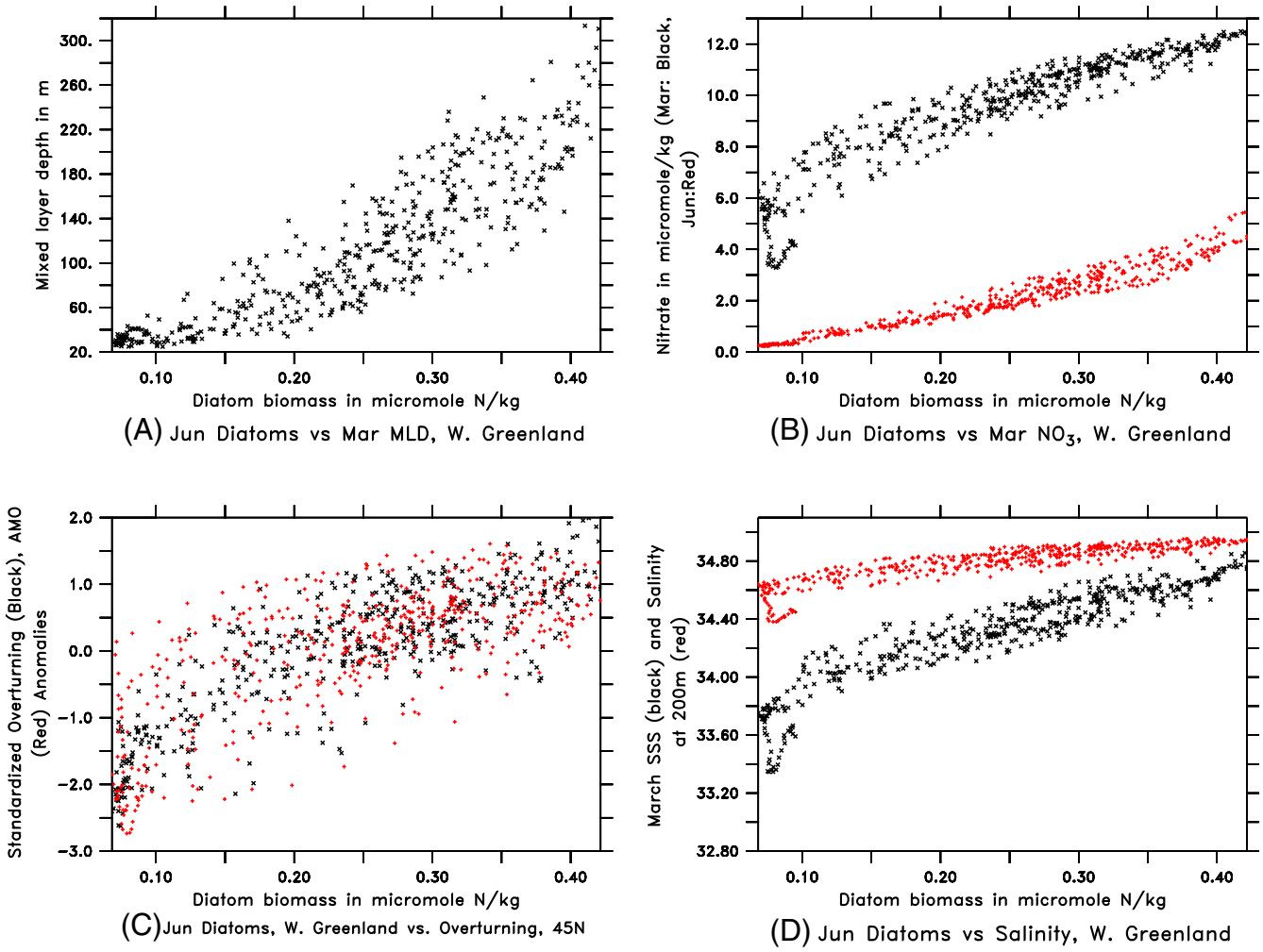

Fig. 11. Scatterplot of decadally smoothed diatom biomass in June for West Greenland in ESM2G. All plots show averages of 50°–60°W and 60°–64°N. (A) March MLD, (B) March NO_3, (C) standardized overturning anomaly at 45 N (black) and standardized AMO index (red) and (D) salinity at surface (black) and 200 m (red).

is used to make the composites than when the AMO index is used. This suggests that, as is the case for the West Greenland coast, it is the variability in the overturning that drives the diatom variability, rather than the (lagged) variation in temperatures.

The driving mechanism for the variability in the Northeast Atlantic in ESM2G is the persistence of higher levels of nitrate into the summer and autumn months. Examination of the nutrient fields shows that this is associated with eastward shifts of the edge of the high-nutrient subpolar gyre. As shown in Fig. 13, high biomass in this region is correlated with a plume of high surface nitrate along the gyre edge (Fig. 13A). These correlations hug the edge of a high nutrient plume (Fig. 13B) down to several hundred meters and are also seen in temperature (Fig. 13C) and density (Fig. 13D). The picture that emerges is one of variations in the central track of high nutrient mode waters in the Northeast Atlantic. As this track broadens and shifts to the east higher nutrients are available to diatoms in surface waters, allowing them to persist through the summer months.

5. Conclusions

We show that Earth System Models are capable of simulating relationships between phytoplankton biomass in various parts of the North Atlantic and the mean temperature of the Atlantic as described by the AMO index. Such relationships however, are likely to be spatially heterogeneous because of the competing impacts of light and nutrient limitation, are further not robust across models, and may be due to the AMO index reflecting changes in circulation. Stronger overturning is associated with more convection and nutrient supply during winter months, but this also suppresses the formation of sea ice, allowing for more shortwave absorption during the spring and warming of the entire region. In the ESM2G model, this increased nutrient supply results in significantly higher diatom biomass throughout the year. Such a relationship between higher salinities, temperatures and biomass is particularly interesting given that there is evidence for significant variability of Atlantic cod populations in this region. Work by Laurel et al. (2008, 2011) on Pacific cod (Gadus macrocephalus) shows that while higher temperatures in the absence of food would be expected to reduce larval survival, higher temperatures in the presence of food produce much larger larval cod at two months past fertilization.

ESM2M, by contrast, does not show strong variability in biomass despite variability in nutrients that has the similar absolute value. This is because nutrients are unrealistically high in this region throughout the year, as mixed-layer light is systematically lower in the level-coordinate model, and so the nutrient variability does not drive significant variability in biomass. Variability in subpolar diatom biomass in ESM2M is in general smaller than in ESM2G and is more tightly related

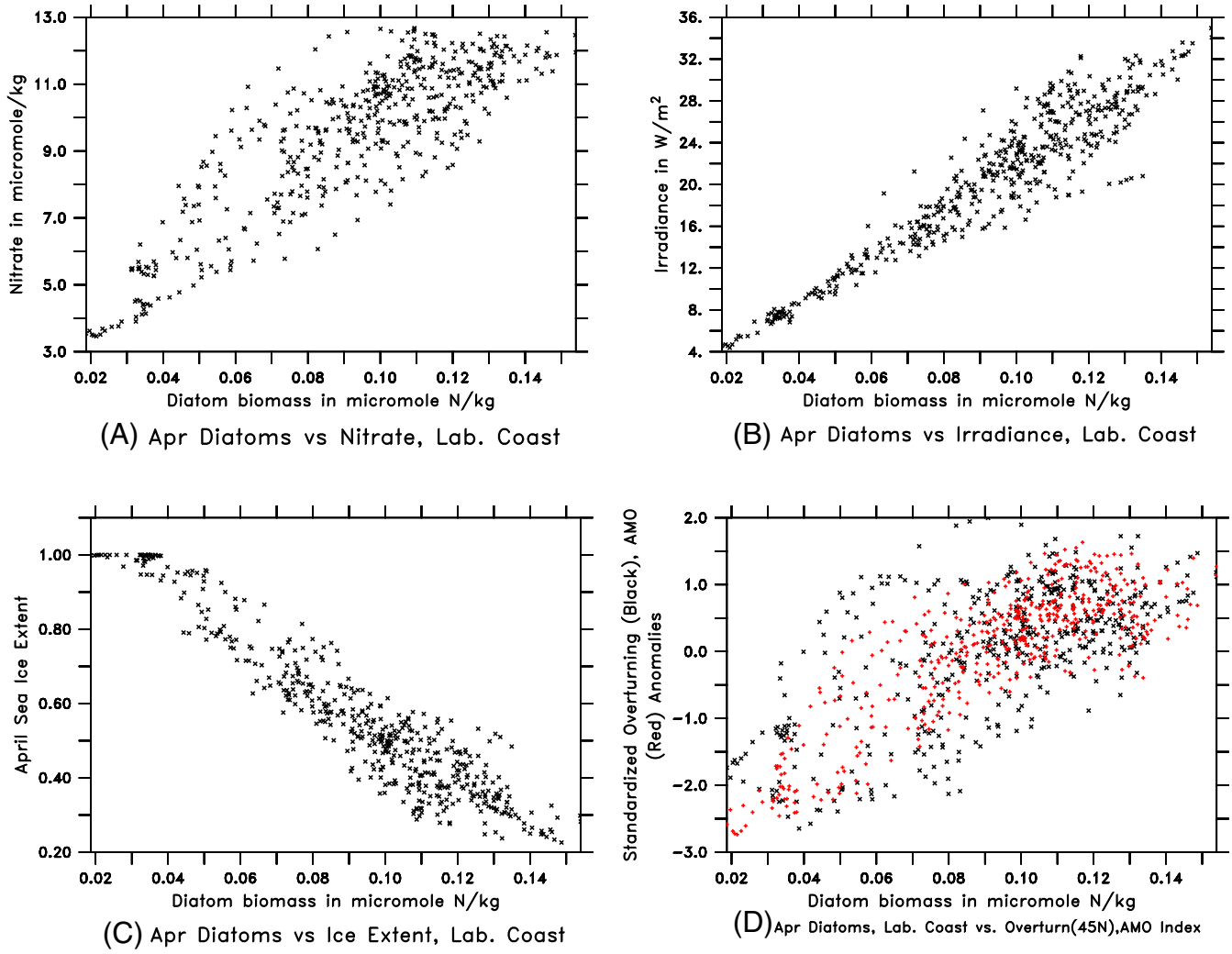

Fig. 12. Relationships between decadally smoothed biomass during the month of April for the coast of Labrador (55°–60°W, 52°–56°N) in ESM2G. (A) April surface nitrate, (B) April irradiance, (C) April sea-ice extent and (D) decadally smoothed overturning in density space at 45°N and the AMO index.

to summertime mixed-layer depth, which in turn is more weakly related to basin-mean SST.

It is unclear which of the two models is "most realistic". On the one hand, the shallower mixed-layers in ESM2G do allow for a more realistic nutrient simulation than in ESM2M. On the other hand, it is possible that these mixed-layers are too sensitive to freshening, and that the shallower mixed-layers in ESM2G yield better nutrients because they compensate for biases in the biogeochemical model. For example, given a different representation of photoadaptation or of light absorption, it is possible that the mean nutrient simulation in ESM2M could be made to look more like ESM2G. Better proxy constraints on sea-ice cover over the entire Holocene (e.g. Solignac et al., 2004), particularly in regions which today are ice-free, would help to constrain this uncertainty. At least one coastal record (Levac, 2001) does suggest the existence of significant intervals during the Holocene where wintertime sea ice extended much further south along the North American coast than it does today, and that such periods were associated with fresh anomalies.

In regions such as West Greenland and the Bay of Biscay, where variability is linked to the overturning rather than to the mean North Atlantic SST, interannual variability may not be a good indicator of the response under global warming. Off West Greenland, warm periods are associated with saltier surface water, deeper convection and more overturning, whereas global warming is expected to warm the Atlantic as a whole, but to decrease overturning and convection. Thus while warm periods in ESM2G are associated with higher productivity, all four of the ESMs studied in Steinacher et al. (2010) show lower productivity under global warming. Such differences highlight the importance of linking biological variability to physical mechanisms (as is done in the statistical analysis of Sarmiento et al., 2004 which considers mixed-layer depths and sea ice cover separately) rather than merely correlating productivity to statistical modes of SST variability.

Both models do show variability in ice-edge regions associated with the AMO index during the spring bloom. These regions do not necessarily vary in the same way as adjoining regions, as illustrated by the Labrador Sea in ESM2G, where the ice edge experiences an earlier bloom but the open-ocean convective region experiences a later spring bloom. We note that these regions may respond to global warming as they do to an increase in the AMO index, and may also represent regions where there is some predictability, insofar as the AMO index lags the overturning circulation at 45°N.

Understanding mechanisms for variability is also important when comparing different models. For example Patara et al. (2011) examine the role of the North Atlantic Oscillation in driving interannual variability in ecosystems within the North Atlantic. Their model finds significant coherence at interdecadal scales between basin averaged SST and SSS, but

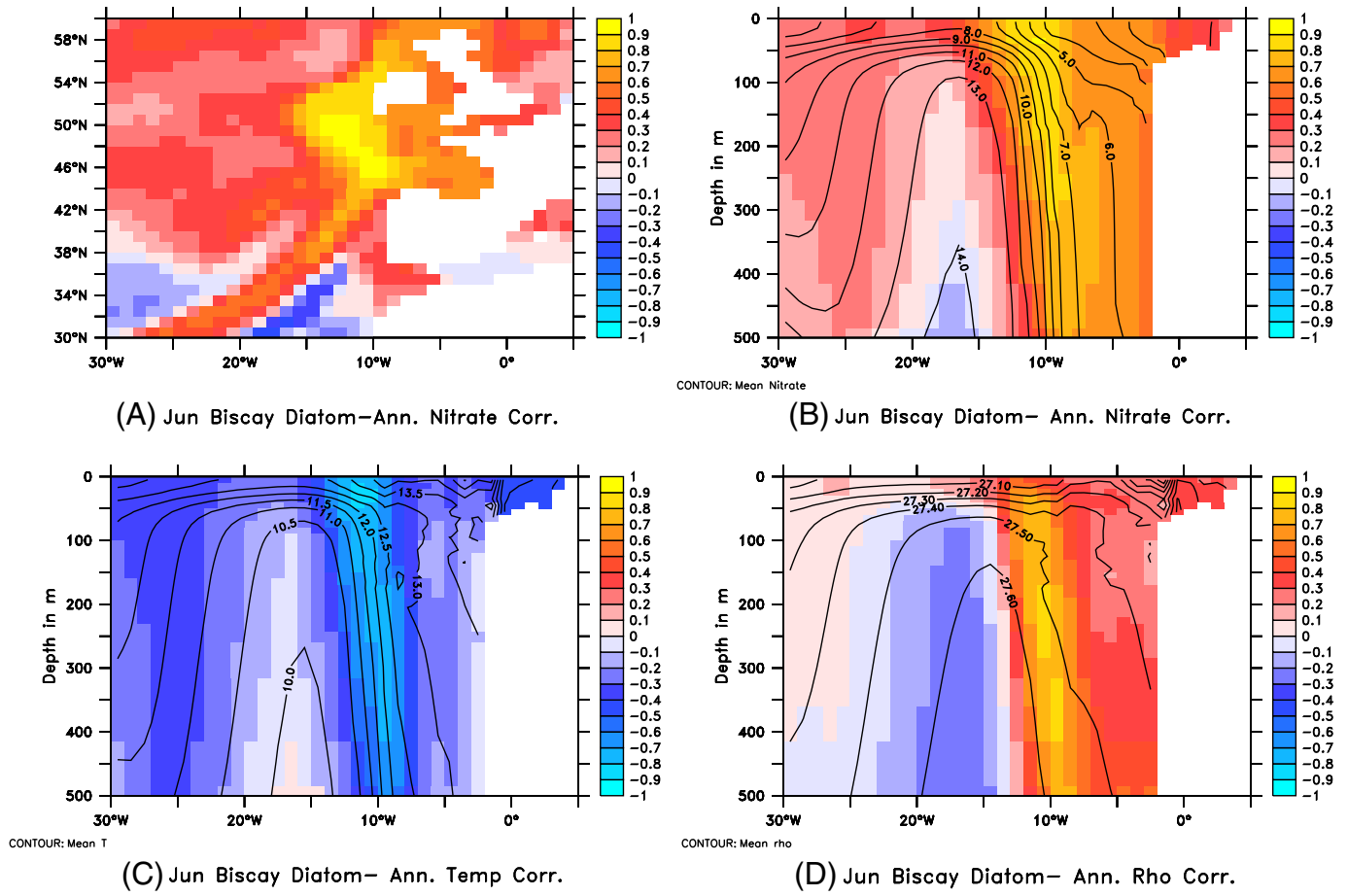

Fig. 13. Relationships between decadally smoothed June diatom biomass above the eastern Biscay plain (10°–12°W, 44°–52°N) and various hydrographic fields. (A) Correlation with decadally smoothed nitrate at surface. (B) Colors: correlation with decadally smoothed annual mean nitrate averaged from 44°–52°N. Contours, mean nitrate 44°–52°N. (C) Colors: correlation with decadally smoothed temperature averaged from 44°–52°N. Contours, mean temperature 44°–52°N. (D) Colors: correlation with decadally smoothed potential density averaged from 44°–52°N. Contours, mean potential density averaged from 44°–52°N.

much less coherence between these two fields and basin-averaged chlorophyll. Instead, they focus on interannual variability associated with the NAO in the center of the subpolar gyre between 45°–60°N and 50°–20°W. This region sees factor of two changes in spring chlorophyll and fall mesozooplankton biomass between positive and negative NAO phases. The differences in biomass are clearly driven by differences in the depth of wintertime mixing and nutrient supply as in our models off of Greenland. However, while the central subpolar gyre does exhibit some interannual variability in diatom biomass in our model, the coefficient of variation is relatively small in ESM2G for both interannual (0.07) and June (0.11) biomass and drops by about half when decadally smoothed. Thus while the AMO/AMOC may play an important role in some regions and models, it is not the dominant driver of ecosystem variability in all regions and models.

The spatial heterogeneity of the biogeochemical response of the Atlantic to changes in overturning (particularly in ESM2G) may help explain why fisheries in different parts of the Atlantic show different responses to interdecadal variability in physical climate. As we have seen in this paper, a stronger AMOC is associated with deeper wintertime convection, resulting in higher nutrients and diatom biomass off of West Greenland, but also in a shift in nutrient fronts resulting in lower diatom biomass off the Bay of Biscay. Thus even though these regions both see warming as a result of increasing AMOC, the biological responses have opposite signs. An additional complication is that the response of organisms at higher trophic levels to such changes in productivity will depend strongly on details of their life history. In particular, organisms whose spawning is tied to particular times of year may be especially susceptible to shifts in the timing of spring or fall blooms. Such details need to be considered by climate scientists in particular when linking variability in their models to observed changes in fisheries.

Acknowledgments

We thank Ron Stouffer, Marie-Aude Pradal, Bob Hallberg, Ken Drinkwater and an anonymous reviewer for comments on earlier versions of this manuscript. AG received support for this work under DOE Grant DE-SC0007066.

References

Belkin, I.S., Levitus, S., Antonov, J., Malmberg, S.-A., 1998. "Great salinity anomalies" in the North Atlantic. Prog. Oceanogr. 41, 1–68.
Collie, J.S., Wood, A.D., Jeffries, H.P., 2008. Long-term shifts in the species composition of a coastal fish community. Can. J. Fish. Aquat. Sci. 65, 1352–1365.
Delworth, T.L., Mann, M.E., 2000. Observed and simulated multidecadal variability in the Northern Hemisphere. Clim. Dyn. 16, 661–676.
Delworth, T.L., Broccoli, A.J., Rosati, A., Stouffer, R.J., Balaji, V., Beesley, J.A., Cooke, W.F., Dixon, K.W., Dunne, J.P., Dunne, K.A., Durachta, J.W., Findell, K.L., Ginoux, P., Gnanadesikan, A., Gordon, C.T., Griffies, S.M., Gudgel, R., Harrison, M.J., Held, I.M., Hemler, R.S., Horowitz, L.W., Klein, S.A., Knutson, T.R., Kushner, P.J., Langenhorst, A.R., Lee, H.-C., Lin, S.-J., Lu, J., Malyshev, S.L., Milly, P.C.D., Ramaswamy, V., Russell, J., Schwartzkopf, M.D., Shevliakova, E., Sirutis, J.J., Spelman, M.J., Stern, W.F., Winton, M.,

Wittenberg, A.T., Wyman, B., Zeng, F., Zhang, R., 2006. GFDL's CM2 global coupled climate models: part 1—formulation and simulation characteristics. J. Clim. 19, 643–674.
Dulvy, N.K., Rogers, S.I., Jennings, S., Stelzenmuller, V., Dye, S.R., Skjoldal, H.R., 2008. Climate change and deepening of the North Sea fish assemblage: a biotic indicator of warming seas. J. Appl. Ecol. 45, 1029–1039. http://dx.doi.org/10.1111/j.1365-2664.2008.01488.
Dunne, J.P., 2013. Technical description of Tracers of Ocean Phytoplankton with Allometric Zooplankton version 2 (TOPAZ2) used in GFDL's ESM2M and ESM2G submitted as part of the Coupled Model Intercomparison Project phase 5. J. Clim. 26. http://dx.doi.org/10.1175/JCLI-D-12-00150.s1 (Suppl. Material).
Dunne, J.P., Armstrong, R.A., Gnanadesikan, A., Sarmiento, J.L., 2005. Empirical and mechanistic models of particle export. Global Biogeochem. Cycles 19, GB4026. http://dx.doi.org/10.1029/2004GB002390.
Dunne, J.P., Sarmiento, J.L., Gnanadesikan, A., 2007. A synthesis of particle export from the surface ocean and cycling through the ocean interior and on the seafloor. Global Biogeochem. Cycles 21, GB4006. http://dx.doi.org/10.1029/2006GB002907.
Dunne, J.P., John, J.G., Adcroft, A.J., Griffies, S.M., Hallberg, R.W., Shevliakova, E.N., Stouffer, R.J., Cooke, W., Dunne, K.A., Harrison, M.J., Krasting, J.P., Levy, H., Malyshev, S.L., Milly, P.C.D., Phillips, P.J., Sentman, L.A., Samuels, B.L., Spelman, M.J., Winton, M., Wittenberg, A.T., Zadeh, N., 2012. GFDL's ESM2 global coupled climate-carbon Earth System Models Part I: physical formulation and baseline simulation characteristics. J. Clim. 15, 6466–6665.
Dunne, J.P., John, J., Shevliakova, E., Stouffer, R.J., Krasting, J.P., Malyshev, S., Milly, P.C.D., Sentman, L., Adcroft, A.J., Cooke, W., Dunne, K.A., Griffes, S.M., Hallberg, R.W., Harrison, M.J., Levy, H., Wittenberg, A.T., Phillips, P.J., Zadeh, N., 2013. GFDL's ESM2 global coupled climate-carbon Earth System Models Part II: carbon system formulation and baseline simulation characteristics. J. Clim. 26, 2247–2267.
Enfield, D.B., Mestaz-Nunez, A.M., Trimble, P.J., 2001. The Atlantic Multidecadal Oscillation and its relation to rainfall and river flows in the continental U.S. Geophys. Res. Lett. 28, 2077–2080.
Ferrari, R., Griffies, S.M., Nurser, A., Vallis, G., 2010. A boundary-value problem for the parameterized mesoscale eddy transport. Ocean Model. 32, 143–156.
Fox-Kemper, B., Danabasoglu, G., Ferrari, R., Griffies, S.M., Hallberg, R.W., Holland, M., Peacock, S., Samuels, B., 2011. Parameterization of mixed layer eddies. III: global implementation and impact on ocean climate simulations. Ocean Model. http://dx.doi.org/10.1016/j.ocemod.2010.09.002.
Garcia, H.E., Locarnini, R.A., Boyer, T.P., Antonov, J.I., 2006. World Ocean Atlas 2005, Volume 4: Nutrients (Phosphate, Nitrate, Silicate). In: Levitus, S. (Ed.), NOAA Atlas NESDIS 64. U.S. Government Printing Office, Washington, D.C. (396 pp.).
Garcia-Soto, C., Pingree, R.D., 2009. Spring and summer blooms of phytoplankton (SeaWiFS/Modis) along a ferry line in the Bay of Biscay and western English Channel. Cont. Shelf Res. 29, 1111–1122.
Gent, P., McWilliams, J.C., 1990. Isopycnal mixing in ocean circulation models. J. Phys. Oceanogr. 20, 150–155.
Gnanadesikan, A., Anderson, W.G., 2009. Ocean water clarity and the ocean general circulation in a coupled climate model. J. Phys. Oceanogr. 39, 314–332.
Gnanadesikan, A., Dixon, K.W., Griffies, S.M., Balaji, V., Barreiro, M., Beesley, J.A., Cooke, W.F., Delworth, T.L., Gerdes, R., Harrison, M.J., Held, I.M., Hurlin, W.J., Lee, H.C., Liang, Z., Nong, G., Pacanowski, R.C., Rosati, A., Russell, J.L., Samuels, B.L., Song, Q., Spelman, M.J., Stouffer, R.J., Sweeney, C., Vecchi, G., Winton, M., Wittenberg, A., Zeng, F., Zhang, R., Dunne, J.P., 2006. GFDL's CM2 global coupled climate models—part 2: the baseline ocean simulation. J. Clim. 19, 675–697.
Gnanadesikan, A., Griffies, S.M., Samuels, B.L., 2007. Effects in a climate model of slope tapering in neutral physics schemes. Ocean Model. 16, 1–16. http://dx.doi.org/10.1016/j.ocemod.2006.06.004.
Gnanadesikan, A., Dunne, J.P., John, J., 2011. What ocean biogeochemical models can tell us about bottom–up control of ecosystem variability. ICES J. Mar. Sci. 68, 1030–1044. http://dx.doi.org/10.1093/icejms/fsr068.
Griffies, S.M., 2009. Elements of MOM4p1: GFDL Ocean Group Technical Report No. 6. NOAA/Geophysical Fluid Dynamics Laboratory, Princeton, USA (444 pp.).
Griffies, S.M., Gnanadesikan, A., Pacanowski, R.C., Larichev, V.D., Dukowicz, J.K., Smith, R.D., 1998. Isoneutral diffusion in a z-coordinate ocean model. J. Phys. Oceanogr. 28, 805–830.
Griffies, S.M., Gnanadesikan, A., Dixon, K.W., Dunne, J.P., Gerdes, R., Harrison, M.J., Rosati, A., Russell, J.L., Samuels, B.L., Spelman, M.J., Winton, M., Zhang, R., 2005. Formulation of an ocean model for global climate simulations. Ocean Sci. 1, 45–79.
Hakkinen, S., Rhines, P., Worthen, D.L., 2011. Atmospheric blocking and Atlantic multidecadal ocean variability. Science 334, 655–659.
Hallberg, R., 1995. Some aspects of the circulation in ocean basins with isopycnals intersecting the sloping boundaries. (Ph.D. thesis) University of Washington (244 pp.).
Hallberg, R., 2003. The suitability of large-scale ocean models for adapting parameterizations of boundary mixing and a description of a refined bulk mixed layer model. Near-Boundary Processes and Their Parameterization: Proc. 'Aha Huliko' a Hawaiian Winter Workshop, Honolulu, HI, University of Hawaii at Manoa, pp. 187–203.
Hallberg, R., Adcroft, A., 2009. Reconciling estimates of the free surface height in Lagrangian vertical coordinate ocean models with mod-split time stepping. Ocean Model. 29, 15–26.
Harrison, M.J., Hallberg, R.W., 2008. Pacific subtropical cell response to reduced equatorial dissipation. J. Phys. Oceanogr. 38, 1894–1912.
Henson, S.J., Dunne, J., Sarmiento, J.L., 2009. Decadal variability in North Atlantic phytoplankton blooms. J. Geophys. Res. Oceans 114, C04013. http://dx.doi.org/10.1029/2008JC005139.
Herweijer, C., Seager, R., Winton, M., Clement, A.C., 2005. Why ocean heat transport warms the global mean climate. Tellus A 57, 662–674.
Hill, B.T., Jones, S.J., 1990. The Newfoundland ice extent and the solar cycle from 1860 to 1988. J. Geophys. Res. 95 (C4), 5385–5394.
Holte, J., Gilson, J., Talley, L., Roemmich, D., 2010. Argo Mixed Layers, Scripps Institution of Oceanography/UCSD. http://mixedlayer.ucsd.edu.
Jensen, A.S., 1939. Concerning a change of climate during recent decades in the arctic and subarctic regions from Greenland in the west to Eurasia in the east, and contemporary biological and geophysical changes. Det Kgl. Danske Vid. Selskab Biol. Meddr, XIV. Einer Munksgard, København 8.
Large, W.G., McWilliams, J.C., Doney, S.C., 1994. Oceanic vertical mixing: a review and a model with a nonlocal boundary layer parameterization. Rev. Geophys. 32, 363–403.
Laurel, B.J., Hurst, T.P., Copeman, L.A., Davis, M.W., 2008. The role of temperature on the growth and survival of early and late hatching Pacific cod larvae (*Gadus macrocephalus*). J. Plankton Res. 30, 1051–1060.
Laurel, B.J., Hurst, T.P., Ciannelli, L., 2011. An experimental examination of temperature interactions in the match–mismatch hypothesis for Pacific cod larvae. Can. J. Fish. Aquat. Sci. 68, 51–61.
Legg, S., Hallberg, R.W., Girton, J.B., 2006. Comparison of entrainment in overflows simulated by z-coordinate, isopycnal and non-hydrostatic models. Ocean Model. 11 (1–2). http://dx.doi.org/10.1016/j.ocemod.2004.11.006.
Levac, E., 2001. High-resolution Holocene paleolynogical record from the Scotia Shelf. Mar. Micropaleontol. 43, 179–197.
Nye, J.A., Link, J.S., Hare, J.A., Overholtz, W.J., 2009. Changing spatial distribution of fish stocks in relation to climate and population size on the Northeast United States continental shelf. Mar. Ecol. Prog. Ser. 393, 111–129.
Patara, L., Visbeck, M., Masina, S., Krahman, G., Vichi, M., 2011. Marine biogeochemical responses to the North Atlantic Oscillation in a coupled climate model. J. Geophys. Res. 116, C07023. http://dx.doi.org/10.1029/2010JC006785.
Rayner, D., Hirschi, J.J.M., Kanzow, T., Johns, W.E., Wright, P.G., Frajka-Williams, E., Bryden, H.L., Meinen, C.S., Baringer, M.O., Marotzke, J., Beal, L.M., Cunningham, S.A., 2011. Monitoring the Atlantic meridional overturning circulation. Deep-Sea Res. II 58, 1744–1753.
Reynolds, R.W., Rayner, N.A., Smith, T.M., Stokes, D.C., Wang, W., 2002. An improved in situ and satellite SST analysis for climate. J. Clim. 15, 1609–1625.
Sarmiento, J.L., Slater, R., Barber, R., Bopp, L., Doney, S.C., Hirst, A.C., Kleypas, J., Matear, R., Mikolajewicz, U., Monfray, P., Soldatov, V., Spall, S.A., Stouffer, R., 2004. Response of ocean ecosystems to climate warming. Global Biogeochem. Cycles 18, GB3003. http://dx.doi.org/10.1029/2003GB002134.
Schlesinger, M.E., Ramankutty, N., 1994. An oscillation in the global climate system of period 65–70 years. Nature 367, 723–726.
Simmons, H.L., Jayne, S.R., St. Laurent, L.C., Weaver, A.J., 2004. Tidally driven mixing in a numerical model of the ocean general circulation. Ocean Model. 6, 245–263.
Solignac, S., de Vernal, A., Hillaire-Marcel, C., 2004. Holocene sea surface conditions in the North Atlantic- contrasted trends and conditions in the western and eastern sectors (Labrador Sea vs. Iceland Basin). Quat. Sci. Rev. 23, 319–334.
Stein, M., 2007. Warming periods off Greenland during 1800–2005: their potential influence on the abundance of Cod (*Gadus morhua*) and Haddock (*Melanogrammus aegelfinus*) in Greenlandic waters. J. Northwest Atl. Fish. Sci. 39, 1–20.
Steinacher, M., Joos, F., Frölicher, T.L., Bopp, L., Cadule, P., Cocco, V., Doney, S.C., Gehlen, M., Lindsay, K., Moore, J.K., Schneider, B., Segschneider, J., 2010. Projected 21st century decrease in marine productivity: a multi-model analysis. Biogeosciences 7, 979–1005. http://dx.doi.org/10.5194/bg-7-979-2010.
Stouffer, R.J., Yin, J., Gregory, J.M., Dixon, K.W., Spelman, M.J., Hurlin, W., Weaver, A.J., Eby, M., Flato, G.M., Hasumi, H., Hu, A., Jungclaus, J.H., Kamenkovich, I.V., Levermann, A., Montoya, M., Murakami, S., Nawrath, S., Oka, A., Peltier, W.R., Robitaille, D.Y., Sokolov, A., Vettoretti, G., Weber, S.L., 2006. Investigating the causes of the response of the thermohaline circulation to past and future climate changes. J. Clim. 19, 1365–1387.
Sundby, S., Nakken, O., 2008. Spatial shifts in spawning habits of Arcto-Norwegian cod related to multidecadal oscillations and climate change. ICES J. Mar. Sci. 65, 953–962.
Sutton, R.T., Hodson, D.L.R., 2005. Atlantic forcing of North American and European summer climate. Science 309, 115–118.
Thiele, G., Sarmiento, J.L., 1990. Tracer dating and ocean ventilation. J. Geophys. Res. 95, 9377–9391. http://dx.doi.org/10.1029/89JC01132.
Ting, M., Kushnir, Y., Seager, R., Li, C., 2011. Robust features of Atlantic multidecadal variability and its impacts. Geophys. Res. Lett. 38, L17705. http://dx.doi.org/10.1029/2011GL048712.
Willebrand, J., Barnier, B., Boning, C., Dieterich, C., Killworth, P.D., LeProvost, C., Jia, Y., Molines, J.-M., New, A.L., 2001. Circulation characteristics in three eddy-permitting models of the North Atlantic. Prog. Oceanogr. 48, 123–161.
Winton, M., Hallberg, R.W., Gnanadesikan, A., 1998. Simulation of density-driven frictional downslope flow in z-coordinate ocean models. J. Phys. Oceanogr. 28 (11), 2163–2174.
Zhang, R., Delworth, T.L., 2006. Impact of Atlantic multidecadal oscillations on India/Sahel rainfall and Atlantic hurricanes. Geophys. Res. Lett. 33, L17712. http://dx.doi.org/10.1029/2006GL026267.